Proton and neutron electromagnetic form factors from lattice QCD

C. Alexandrou[1,2], S. Bacchio[1], M. Constantinou[3], J. Finkenrath[2]
K. Hadjiyiannakou[2], K. Jansen[4], G. Koutsou[2], and A. Vaquero Aviles-Casco[5]
[1]*Department of Physics, University of Cyprus, P.O. Box 20537, 1678 Nicosia, Cyprus*
[2]*Computation-based Science and Technology Research Center, The Cyprus Institute, 20 Kavafi Str., Nicosia 2121, Cyprus*
[3]*Department of Physics, Temple University, 1925 N. 12th Street, Philadelphia, PA 19122-1801, USA*
[4]*NIC, DESY, Platanenallee 6, D-15738 Zeuthen, Germany*
[5]*Department of Physics and Astronomy, University of Utah, Salt Lake City, UT 84112, USA*

The electromagnetic form factors of the proton and the neutron are computed within lattice QCD using simulations of maximally twisted mass fermions with masses fixed to their physical values. We analyze two new ensembles of $N_f = 2$ and $N_f = 2 + 1 + 1$ and use several values of the sink-source time separation in the range of 1.0 fm to 1.6 fm to ensure ground state identification. The light quark disconnected contributions are evaluated to very high accuracy enabling us to include them in the determination of the proton and neutron form factors, the electric and magnetic radii, and the magnetic moments. We find that disconnected contributions are non-negligible and contribute up to 15% for the case of the neutron electric charge radius.

PACS numbers: 11.15.Ha, 12.38.Gc, 24.85.+p, 12.38.Aw, 12.38.-t
Keywords: Nucleon structure, Nucleon electromagnetic form factors, Disconnected, Lattice QCD

I. INTRODUCTION

Nucleons, being composite particles, have a non-trivial internal structure that can be probed by measuring their electromagnetic form factors. Despite having been extensively studied both theoretically and experimentally, there is still interest in obtaining these quantities at higher precision and over a wider range of momentum transfers. The proton electric form factor is extracted to high precision from electron proton scattering [1]. Its slope at vanishing momentum transfer squared yields the proton charge root mean square (r.m.s) radius. Prior to 2010, the charge r.m.s. radius of the proton was considered a well-determined quantity (see Ref. [2] for a recent review). A pioneering experiment using Lamb shifts in muonic hydrogen surprisingly found a value smaller by five standard deviations [3], triggering the so-called proton radius puzzle. The origin of this discrepancy is not yet understood, and potential systematic uncertainties related to the analysis methodologies in the two types of experiments have not been excluded. Another quantity of interest is the neutron electric form factor [4], which is accessed indirectly experimentally through electron-deuteron or electron-helium scattering and therefore remains poorly-known. It is of substantial importance to compute these fundamental quantities from first principles, and lattice QCD, with simulations at physical values of the QCD parameters, provides an ideal formulation for such an investigation.

Within this work, we compute the proton and neutron electromagnetic form factors including light quark disconnected contributions. We use an ensemble of twisted mass fermions with two degenerate light quarks, a strange and a charm quark (N_f=2+1+1) with masses fixed to their physical value (referred to hereafter as physical point). A clover term is added to the action to suppress isospin breaking effects that come quadratically with the lattice spacing. Details on the simulation can be found in Ref. [5]. In addition, we present an analysis of a twisted mass ensemble of two degenerate light quarks with masses fixed to their physical values ($N_f = 2$) to assess finite volume artifacts by comparing to previous results obtained using an $N_f = 2$ ensemble with a smaller volume and same pion mass and lattice spacing [6, 7]. Comparison between $N_f = 2$ and $N_f = 2 + 1 + 1$ also sheds light on any possible unquenching effects of the strange and charm quarks. The momentum dependence of the form factors is fitted using two Ansätze, namely either a dipole or the Galster-like parameterization [8] and the model independent z-expansion [9]. The fits allow for the extraction of the magnetic moment and the electric and magnetic r.m.s radii of the proton and neutron and provide a measure of the systematics due to choice of the fit method.

A crucial component of our analysis is the use of hierarchical probing [10] combined with deflation of the lower lying eigenvalues [11] that enables us to calculate the light quark disconnected contributions to the form factors at an unprecedented accuracy at the physical point. This allows us to obtain the proton and neutron form factors at the physical point without neglecting disconnected contributions.

The remainder of this paper is organized as follows: In Section II, we describe the nucleon matrix elements required to extract the electromagnetic form factors and in Section III we provide details on the lattice QCD techniques employed for the computation of the connected and disconnected diagrams. In Section IV, we discuss the analysis of the data paying particular attention to the identification of the ground state matrix element. We include an assessment of finite volume and unquenching effects using results from two N_f=2 ensembles. In Sec-

tion V, we fit the isovector and isoscalar form factors to extract the magnetic moments and radii. We compare to other lattice QCD studies using simulations close to physical pion masses in Section VI [12–15]. Our final results for the proton and neutron electromagnetic form factors are given in Section VII. Finally, in Section VIII, we summarize our findings and conclude. For completeness, we include in Appendix A the decomposition of the nucleon matrix elements in terms of the form factors and in Appendix B a table with the numerical results for the electric and magnetic form factors as a function of the square of the momentum transfer.

II. ELECTROMAGNETIC FORM FACTORS

The nucleon matrix element of the electromagnetic current is parameterized in terms of the Dirac (F_1) and Pauli (F_2) form factors given in Minkowski space by,

$$\langle N(p',s')|j_\mu|N(p,s)\rangle = \sqrt{\frac{m_N^2}{E_N(\vec{p}\,')E_N(\vec{p})}}\times \bar{u}_N(p',s')\left[\gamma_\mu F_1(q^2)+\frac{i\sigma_{\mu\nu}q^\nu}{2m_N}F_2(q^2)\right]u_N(p,s)\,. \quad (1)$$

$N(p,s)$ is the nucleon state with initial (final) momentum p (p') and spin s (s'), with energy $E_N(\vec{p})$ ($E_N(\vec{p}\,')$) and mass m_N. $q^2{\equiv}q_\mu q^\mu$ is the momentum transfer squared $q_\mu{=}(p'_\mu - p_\mu)$, u_N is the nucleon spinor and j_μ is the vector current. The local vector current is given by,

$$j_\mu = \sum_f e_f\, j_\mu^f = \sum_f e_f\, \bar{q}_f\gamma_\mu q_f\,, \quad (2)$$

where q_f and e_f is the quark field of flavor f and its electric charge respectively and the summation runs over all the quark flavors. We use the symmetrized lattice conserved vector current given by

$$\begin{aligned} j_\mu^f(x) = \frac{1}{4}\ [\ &\bar{q}_f(x+\hat{\mu})U_\mu^\dagger(x)(1+\gamma_\mu)q_f(x)\\ &-\bar{q}_f(x)U_\mu(x)(1-\gamma_\mu)q_f(x+\hat{\mu})\\ &+\bar{q}_f(x)U_\mu^\dagger(x-\hat{\mu})(1+\gamma_\mu)q_f(x-\hat{\mu})\\ &-\bar{q}_f(x-\hat{\mu})U_\mu(x-\hat{\mu})(1-\gamma_\mu)q_f(x)\ ]\,, \end{aligned}$$

which, unlike the local vector current, does not need renormalization. The electric and magnetic Sachs form factors $G_E(q^2)$ and $G_M(q^2)$ are alternative Lorentz invariant quantities and are expressed in terms of $F_1(q^2)$ and $F_2(q^2)$ via the relations,

$$G_E(q^2) = F_1(q^2) + \frac{q^2}{4m_N^2}F_2(q^2)\,, \quad (3)$$

$$G_M(q^2) = F_1(q^2) + F_2(q^2)\,. \quad (4)$$

In the isospin limit, where the up and down quarks are degenerate, we consider the isovector combination $\langle p|j_\mu^u - j_\mu^d|p\rangle$ that gives the difference between the proton and neutron form factors and the isoscalar combination $\langle p|j_\mu^u + j_\mu^d|p\rangle/3$ for the sum of the proton and neutron form factors. The electric form factor at zero momentum yields the nucleon charge, i.e. $G_E^p(0){=}1$ and $G_E^n(0){=}0$ which, when using the lattice conserved current, holds by symmetry, even prior gauge averaging. The magnetic form factor at $q^2{=}0$ gives the magnetic moment, while the radii can be extracted from the slope of the electric and magnetic form factors as $q^2\to 0$, namely:

$$\langle r^2\rangle = \frac{-6}{G(0)}\frac{\partial G(q^2)}{\partial q^2}\Big|_{q^2=0}\,. \quad (5)$$

III. CALCULATION ON THE LATTICE

A. Nucleon matrix element

Extraction of nucleon matrix elements within the lattice QCD formulation requires the evaluation of two- and three-point correlation functions in Euclidean space. We thus give all quantities in Euclidean space from here on. We use the standard nucleon interpolating field

$$J_N(\vec{x},t) = \epsilon^{abc}u^a(x)[u^{b\intercal}(x)\mathcal{C}\gamma_5 d^c(x)]\,, \quad (6)$$

where u and d are up- and down-quark spinors and $\mathcal{C}{=}\gamma_0\gamma_2$ is the charge conjugation matrix. The two-point function in momentum space is given by

$$C(\Gamma_0,\vec{p};t_s,t_0){=}\sum_{\vec{x}_s}\mathrm{Tr}\left[\Gamma_0\langle J_N(t_s,\vec{x}_s)\bar{J}_N(t_0,\vec{x}_0)\rangle\right]e^{-i(\vec{x}_s-\vec{x}_0)\cdot\vec{p}}\,, \quad (7)$$

and the three-point function is given by

$$C_\mu(\Gamma_\nu,\vec{q},\vec{p}\,';t_s,t_{\rm ins},t_0){=}\sum_{\vec{x}_{\rm ins},\vec{x}_s}e^{i(\vec{x}_{\rm ins}-\vec{x}_0)\cdot\vec{q}}e^{-i(\vec{x}_s-\vec{x}_0)\cdot\vec{p}\,'}\times \mathrm{Tr}\left[\Gamma_\nu\langle J_N(t_s,\vec{x}_s)j_\mu(t_{\rm ins},\vec{x}_{\rm ins})\bar{J}_N(t_0,\vec{x}_0)\rangle\right] \quad (8)$$

The initial position and time (x_0) is referred to as the *source*, the position and time of the current j_μ is ($x_{\rm ins}$) as the *insertion* and the final position (x_s) as the *sink*. Γ_ν is a projector acting on spin indices, with $\Gamma_0{=}\frac{1}{2}(1{+}\gamma_0)$ yielding the unpolarized and $\Gamma_k{=}\Gamma_0 i\gamma_5\gamma_k$ the polarized matrix elements. Inserting complete sets of states in Eq. (8), one obtains the nucleon matrix element as well as additional matrix elements of higher energy states with the quantum numbers of the nucleon multiplied by overlap terms and time dependent exponentials. For large enough time separations, the excited state contributions are suppressed compared to the nucleon ground state and one can then extract the desired matrix element. To increase the overlap of the interpolating field with the nucleon ground state, so that excited states are suppressed at earlier time separations, we use Gaussian smeared point sources [16, 17] with 125 steps and parameter $\alpha_G{=}0.2$ and we smear the gauge links which enter

the Gaussian smearing operator with APE [18] smearing, using 50 steps and α_{APE}=0.5. An optimized ratio [19–21] of the three-point function over a combination of two-point functions is used to cancel time dependent exponentials and overlaps, given by

$$R_\mu(\Gamma_\nu,\vec{p}\,',\vec{p};t_s,t_{\rm ins}) = \frac{C_\mu(\Gamma_\nu,\vec{p}\,',\vec{p};t_s,t_{\rm ins})}{C(\Gamma_0,\vec{p}\,';t_s)} \times \sqrt{\frac{C(\Gamma_0,\vec{p};t_s-t_{\rm ins})C(\Gamma_0,\vec{p}\,';t_{\rm ins})C(\Gamma_0,\vec{p}\,';t_s)}{C(\Gamma_0,\vec{p}\,';t_s-t_{\rm ins})c(\Gamma_0,\vec{p};t_{\rm ins})C(\Gamma_0,\vec{p};t_s)}}\,, \quad (9)$$

where t_s and $t_{\rm ins}$ are taken to be relative to the source t_0 for simplicity. In the limit of large time separations, $(t_s-t_{\rm ins}) \gg 1$ and $t_{\rm ins} \gg 1$, the lowest state dominates and the ratio becomes time independent

$$R_\mu(\Gamma_\nu;\vec{p}\,',\vec{p};t_s;t_{\rm ins}) \xrightarrow[t_{\rm ins}\gg 1]{t_s-t_{\rm ins}\gg 1} \Pi_\mu(\Gamma_\nu;\vec{p}\,',\vec{p})\,. \quad (10)$$

$G_E(Q^2)$ and $G_M(Q^2)$ are extracted from linear combinations of $\Pi_\mu(\Gamma_\nu;\vec{p}\,',\vec{p})$ as expressed in Appendix A, with $Q^2 \equiv -q^2$ the Euclidean momentum transfer squared.

Contracting the quark fields in Eq. (8) gives rise to two types of diagrams depicted in Fig. 1, namely the so-called connected and disconnected contributions. In the case of

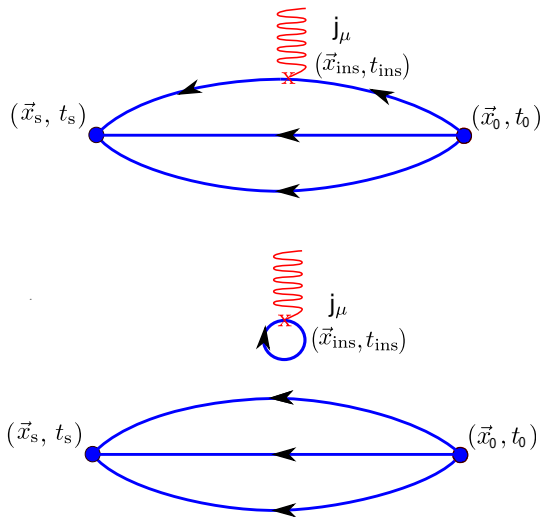

FIG. 1. Connected (upper panel) and disconnected (lower panel) contributions to the nucleon three-point function, with the source at x_0, the sink at x_s and the current insertion (j_μ) at $x_{\rm ins}$.

the connected diagram, the insertion operator couples to a valence quark and an all-to-all propagator arises between sink and insertion. We use sequential inversions through the sink that require keeping the sink-source time separation t_s, the projector, and the sink momentum $\vec{p}\,'$ fixed. We perform additional sets of inversions to compute the three-point function for several values of t_s, for both the unpolarized and polarized projectors, setting $\vec{p}\,'=\vec{0}$. We use an appropriately tuned multigrid algorithm [22–24] for the efficient inversion of the Dirac operator entering in the computation of the connected diagram. The disconnected diagram involves the disconnected quark loop correlated with the nucleon two-point correlator. The disconnected quark loop is given by

$$L(t_{\rm ins},\vec{q}) = \sum_{\vec{x}_{\rm ins}} {\rm Tr}\left[D^{-1}(x_{\rm ins};x_{\rm ins})\mathcal{G}\right] e^{i\vec{q}\cdot\vec{x}_{\rm ins}} \quad (11)$$

where $D^{-1}(x_{\rm ins};x_{\rm ins})$ is the quark propagator which starts and ends at the same point $x_{\rm ins}$ and $\mathcal{G}$ is a general γ-structure, which for this work is the vector current. A direct computation of quark loops would need inversions from all-to-all spatial points on the lattice, making the evaluation unfeasible for our lattice size. We therefore employ stochastic techniques to estimate it combined with dilution schemes [25] that take into account the sparsity of the Dirac operator and its decay properties. Namely, in this work, we employ the *hierarchical probing* technique [10], which provides a partitioning scheme that eliminates contributions from neighboring points in the trace of Eq. 11 up to a certain distance 2^k. Using Hadamard vectors as the basis vectors for the partitioning, one needs $2^{d*(k-1)+1}$ vectors, where d=4 for a 4-dimensional partitioning. Note that the computational resources required are proportional to the number of Hadamard vectors, and therefore in d=4 dimensions increase 16-fold each time the probing distance increases by one. Contributions entering from points beyond the probing distance are expected to be suppressed due to the exponential decay of the quark propagator and are treated with standard noise vectors which suppress all off-diagonal contributions by $1/\sqrt{N_r}$, i.e.

$$\frac{1}{N_r}\sum_r |\xi_r\rangle\langle\xi_r| = 1 + \mathcal{O}\left(\frac{1}{\sqrt{N_r}}\right), \quad (12)$$

where N_r is the size of the stochastic ensemble. Hierarchical probing has been employed with great success in previous studies [26, 27] for an ensemble with a pion mass of 317 MeV. For simulations at the physical point, it is expected that a larger probing distance is required since the light quark propagator decays more slowly at smaller quark masses. We avoid the need of increasing the distance by combining hierarchical probing with deflation of the low modes [11], namely we construct the low mode contribution to the light quark loops by computing exactly the 200 smallest eigenvalues and corresponding eigenvectors of the squared Dirac operator and combine with the contribution from the remaining modes which are estimated using hierarchical probing. Additionally, we employ the *one-end trick* [28], used in our previous studies [29–32] and fully dilute in spin and color.

B. Gauge Ensembles and Statistics

For the extraction of the electromagnetic form factors we analyze one N_f=2+1+1 ensemble [5] and one

$N_f = 2$ ensemble. For both ensembles the quark masses are tuned to their physical values. The fermion action is the twisted mass fermion action with a clover term. Automatic $\mathcal{O}(a)$ improvement is achieved by tuning to maximal twist [33, 34]. The $N_f = 2 + 1 + 1$ ensemble is simulated using a lattice of $64^3 \times 128$, lattice spacing $a = 0.0809(2)(4)$ fm, pion mass $m_\pi = 138(1)$ MeV, and Lm_π=3.62 [5]. To assess finite volume effects, we use two N_f=2 ensembles, which only differ in their volume, namely one has $Lm_\pi = 2.98$ and the other Lm_π=3.97 while both have pion mass 130(1) MeV and a=0.0938(3)(1) fm. Results for the former ensemble are from Refs. [5, 7] while results for the latter are reported here for the first time. The simulation parameters are tabulated in Table I.

TABLE I. Simulation parameters for the N_f=2+1+1 [5] and N_f=2 [35] ensembles used in this work.

$c_{\rm SW}$	β	N_f	a [fm]	Vol.	m_π [MeV]	$m_\pi L$	m_N [MeV]	m_N/m_π	L [fm]
1.69	1.778	2+1+1	0.0809(2)(4)	$64^3\times128$	138(1)	3.62	941(2)	6.83(2)	5.18
1.57551	2.1	2	0.0938(3)(1)	$48^3\times96$	130(1)	2.98	932(4)	7.10(4)	4.52
1.57551	2.1	2	0.0938(3)(1)	$64^3\times128$	130(2)	3.97	929(6)	7.14(4)	6.02

For the analysis of the N_f=2+1+1 ensemble we use 750 configurations separated by 4 trajectories. For the connected contributions we evaluate the three-point function for five sink-source time separations in the range 0.97 fm to 1.62 fm increasing the number of source positions per configuration as we increase the time separation so as to keep the statistical error approximately constant. In Table II we give the statistics used in the calculation of the connected three-point functions.

TABLE II. Statistics for the evaluation of the connected three-point functions for the N_f=2+1+1 ensemble. Columns from left to right are the sink-source time separations, the number of configurations analyzed, the number of source positions per configuration chosen randomly and the total number of measurements for each time separation.

t_s/a	$N_{\rm cnfs}$	$N_{\rm srcs}$	$N_{\rm meas}$
12	750	4	3000
14	750	6	4500
16	750	16	12000
18	750	48	36000
20	750	64	48000

For the evaluation of the disconnected contributions we use $N_{\rm srcs} = 200$ source positions to generate the nucleon two-point functions that are correlated with the quark loop to produce the disconnected contribution to the three-point function. We find that the volume is sufficiently large so that the data extracted from this large number of randomly distributed source positions on the same configuration is statistically independent. Nevertheless, we average over all source positions for each configuration and take the averaged correlation function as one statistic in our jackknife error analysis. As mentioned in the previous section, for the evaluation of the light quark loops we use the first 200 low modes of the squared Dirac operator to reconstruct exactly part of the loop. The contribution from the high modes is estimated stochastically using one noise vector per configuration combining hierarchical probing, one-end trick and spin-color dilution. For the hierarchical probing we use distance eight coloring resulting in 512 Hadamard vectors, which combined with spin-color dilution leads to 6144 inversions per configuration. We note that the next coloring distance would demand 8192 Hadamard vectors, resulting in 98304 inversions per configurations after combining with spin-color dilution, making such a computation more than an order of magnitude more expensive. Table III summarizes the parameters for the computation of the disconnected three-point functions.

TABLE III. Details on the set-up for the evaluation of the light disconnected diagrams. $N_{\rm cnfs}$ is the number of configurations analyzed, $N_{\rm def}$ is the number of low modes we deflate, N_r the number of noise vectors, and $N_{\rm Had}$ the number of Hadamard vectors. $N_{\rm sc}$ corresponds to spin-color dilution and $N_{\rm inv}$/conf is the total number of inversions per configuration. $N_{\rm srcs}$ is the number of randomly distributed smeared point sources per configuration used to obtain the nucleon two-point functions and $N_{\rm meas}$ the total number of measurements.

	Loops					Two-point	
$N_{\rm cnfs}$	$N_{\rm def}$	N_r	$N_{\rm Had}$	$N_{\rm sc}$	$N_{\rm inv}$/conf	$N_{\rm srcs}$	$N_{\rm meas}$
750	200	1	512	12	6144	200	150000

The N_f=2, $64^3 \times 128$ ensemble is used to check for finite volume effects, comparing the connected contributions to those of the N_f=2, $48^3 \times 96$ ensemble. For the latter, the setup is reported in Ref. [7] and summarized in

Table I. For the former, larger lattice, we analyze three sink-source time separations in the range of 1.1 fm to 1.5 fm. We fix the number of source positions per configuration to 16 and we analyze more configurations for higher separations to control statistical error. In Table IV we summarize the statistics.

TABLE IV. Statistics for the evaluation of the connected three-point functions for the N_f=2, $64^3 \times 128$ ensemble. The notation is as in Table II.

t_s/a	$N_{\rm cnfs}$	$N_{\rm srcs}$	$N_{\rm meas}$
12	333	16	5328
14	515	16	8240
16	1040	16	16640

C. Excited states contamination

Assessment of excited state effects is imperative for the proper extraction of the desirable nucleon matrix element. However, ensuring ground state dominance is a delicate process due to the exponentially increasing statistical noise with the sink-source separation. We use four methods to study the effect of excited states and identify the final results based on a critical comparison among these methods. Only by employing these different methods can one reach a reliable assessment of excited state contributions and extract the nucleon matrix element of interest. The methods employed are as follows:

Plateau method: In this method we use the ratio in Eq. (9) and identify a time-independent window (plateau) as we increase t_s. The converged plateau value then yields the desired matrix element.

Two-state method: Within this method we fit the two- and three-point functions considering contributions up to the first excited state using the expressions

$$C(\vec{p},t_s) = c_0(\vec{p})e^{-E_0(\vec{p})t_s} + c_1(\vec{p})e^{-E_1(\vec{p})t_s}\,, \qquad (13)$$

$$\begin{aligned} &C_\mu(\Gamma_\nu,\vec{p}\,',\vec{p},t_s,t_{\rm ins}) = \\ &A^\mu_{00}(\Gamma_\nu,\vec{p}\,',\vec{p})e^{-E_0(\vec{p}\,')(t_s-t_{\rm ins})-E_0(\vec{p})t_{\rm ins}} \\ &+ A^\mu_{01}(\Gamma_\nu,\vec{p}\,',\vec{p})e^{-E_0(\vec{p}\,')(t_s-t_{\rm ins})-E_1(\vec{p})t_{\rm ins}} \\ &+ A^\mu_{10}(\Gamma_\nu,\vec{p}\,',\vec{p})e^{-E_1(\vec{p}\,')(t_s-t_{\rm ins})-E_0(\vec{p})t_{\rm ins}} \\ &+ A^\mu_{11}(\Gamma_\nu,\vec{p}\,',\vec{p})e^{-E_1(\vec{p}\,')(t_s-t_{\rm ins})-E_1(\vec{p})t_{\rm ins}}. \end{aligned} \qquad (14)$$

In Eqs. (13) - (14) $E_0(\vec{p})$ and $E_1(\vec{p})$ are the energies of the ground and first excited state with total momentum $\vec{p}$, respectively. Fitting simultaneously the two- and three-point functions involves twelve parameters. Note that for non-zero momentum transfer, $A^\mu_{01}(\Gamma_\nu,\vec{p}\,',\vec{p}) \neq A^\mu_{10}(\Gamma_\nu,\vec{p}\,',\vec{p})$. The desired nucleon matrix element is obtained from

$$\Pi_\mu(\Gamma_\nu;\vec{p}\,',\vec{p}) = \frac{A^\mu_{00}(\Gamma_\nu,\vec{p}\,',\vec{p})}{\sqrt{c_0(\vec{p}\,')c_0(\vec{p})}}. \qquad (15)$$

Summation method: Summing over $t_{\rm ins}$ in the ratio of Eq. (9) yields a geometric sum [36, 37] from which we obtain,

$$\begin{aligned} R^{sum}_\mu(\Gamma_\nu;\vec{p}\,',\vec{p};t_s) = \sum_{t_{\rm ins}=a}^{t_s-a} R_\mu(\Gamma_\nu;\vec{p}\,',\vec{p};t_s;t_{\rm ins}) = \\ c + \Pi_\mu(\Gamma_\nu;\vec{p}\,',\vec{p})\times t_s + \cdots \end{aligned} \qquad (16)$$

where the ground state contribution, $\Pi_\mu(\Gamma_\nu;\vec{p}\,',\vec{p})$, is extracted from the slope of a linear fit with respect to t_s. The sink-source time separation t_s considered in the fit should be large enough to suppress higher excited states.

Derivative Summation method: Instead of performing a linear fit in Eq. (16) to extract the matrix element, one can take finite differences to the summed ratio [38] as follows

$$\begin{aligned} &dR^{sum}_\mu(\Gamma_\nu;\vec{p}\,',\vec{p};t_s) = \\ &\frac{R^{sum}_\mu(\Gamma_\nu;\vec{p}\,',\vec{p};t_s+dt_s) - R^{sum}_\mu(\Gamma_\nu;\vec{p}\,',\vec{p};t_s)}{dt_s} \end{aligned} \qquad (17)$$

and fit to a constant to extract the desired matrix element.

D. Momentum dependence fits of form factors

Electromagnetic form factors are described by the nucleon matrix element of the vector current, and assuming vector meson pole dominance for $Q^2 < 0$, one expects that for small $Q^2 > 0$ the behavior will be dominated by the poles in the time-like region. One would then expect a dipole form given by [39]

$$G(Q^2) = \frac{G(0)}{(1+\frac{Q^2}{M^2})^2}, \qquad (18)$$

where M is the mass of the vector meson that parameterizes the Q^2 dependence. The value of the form factor at zero momentum transfer gives the electric charge in the case of the electric form factor and the magnetic moment in the case of the magnetic form factor. Combining Eq. (18) and Eq. (5) one can relate M to the mean square radius as

$$\langle r^2\rangle = \frac{12}{M^2}. \qquad (19)$$

The neutron electric form factor and disconnected contributions to the electric form factors are zero for Q^2=0 and we treat them as a special cases, fitting them using the Galster-like parameterization [8, 40], given by

$$G(Q^2) = \frac{Q^2 A}{4m_N^2 + Q^2 B}\frac{1}{(1+\frac{Q^2}{0.71{\rm GeV}^2})^2}, \qquad (20)$$

with A, B fit parameters and m_N the nucleon mass. In this case the radius is given by

$$\langle r^2 \rangle = -\frac{3A}{2m_N^2}. \tag{21}$$

Another fit form, which has been applied recently to experimental data of both electromagnetic and axial form factors, is the model independent z-expansion [9]. In this case, the form factor is expanded in a series given by,

$$G(Q^2) = \sum_{k=0}^{k_{\rm max}} a_k z^k, \tag{22}$$

where

$$z = \frac{\sqrt{t_{\rm cut}+Q^2} - \sqrt{t_{\rm cut}}}{\sqrt{t_{\rm cut}+Q^2} + \sqrt{t_{\rm cut}}} \tag{23}$$

and $t_{\rm cut}$ is the time-like cut of the form factor. We take $t_{\rm cut}$=$4m_\pi^2$ for the isovector combination $G^u - G^d$ and $t_{\rm cut}$=$9m_\pi^2$ for the isoscalar combination $G^u + G^d$ [9]. For convergence of the truncated series of Eq. (22) the coefficients a_k should be bounded in size and convergence should be demonstrated by increasing $k_{\rm max}$. The interested reader is referred to Ref. [6] for details about our procedure. The mean square radius is given by

$$\langle r^2 \rangle = -\frac{3a_1}{2a_0 t_{cut}}, \tag{24}$$

while the value of the form factor at zero momentum transfer is $G(0)$=a_0.

IV. ANALYSIS OF LATTICE RESULTS

A. Isovector and connected isoscalar form factors

The isovector combination gives the difference between the proton and neutron form factors, and in this case, only the connected diagram contributes since disconnected contributions cancel up to cut-off effects. For the connected diagram we use a frame where the nucleon final momentum is zero, thus $\vec{q}$=$-\vec{p}$.

In Figs. 2 and 3 we show the ratios defined in Eq. (9) as a function of the sink-source time separation, and for three values of the momentum transfer squared, that is for Q^2=0.056 GeV^2, Q^2=0.216 GeV^2 and Q^2=0.547 GeV^2. In a frame where the nucleon final momentum is zero, the expression given in Eq. (A1) and Eq. (A2) reduce to Eqs. (A4,A5), and (A6) in Appendix A, giving separately the electric and magnetic form factors. In the case of $G_E^{u-d}(Q^2)$ the plateau value decreases as t_s increases with the effect becoming larger as Q^2 increases showing that at larger Q^2 values contamination due to excited states is more severe. In the case of $G_M(Q^2)$, excited states are suppressed and only a small variation is observed.

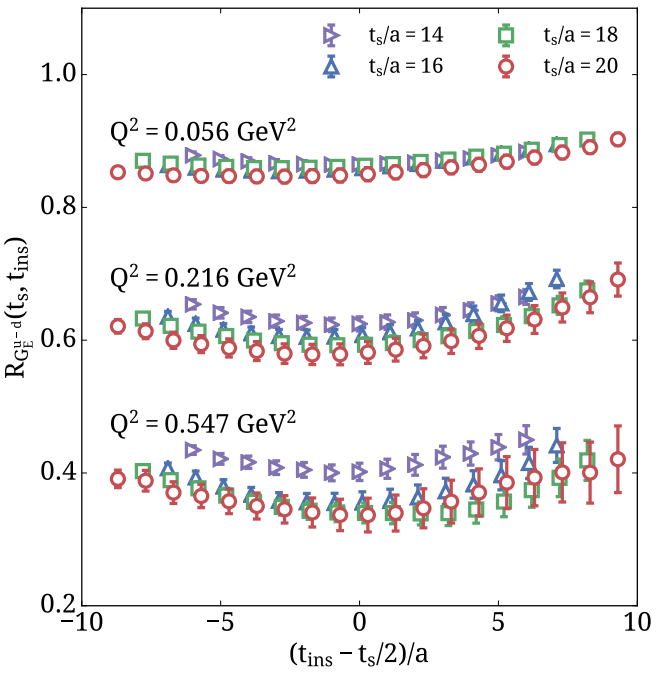

FIG. 2. Ratio yielding the isovector electric form factor. The sink-source time separations are t_s/a=14 (right triangles), t_s/a=16 (triangles), t_s/a=18 (squares) and t_s/a=20 (circles). We present the ratio for three Q^2 values, namely 0.056, 0.216 and 0.547 GeV^2, from top to bottom.

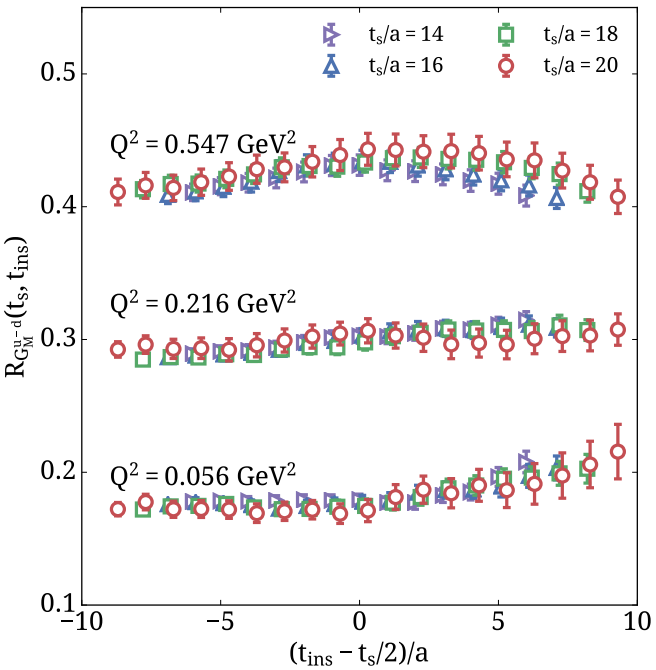

FIG. 3. Ratio yielding the isovector magnetic form factor. The notation is the same as in Fig. 2.

We further investigate effects due to excited states by employing the summation and two-state fits. In Fig. 4

we show linear fits to the summed ratio for three different values of Q^2. The slope of the lines gives the nucleon matrix element. All three momenta follow well the linear behavior, within the statistical error, indicating that contributions from higher order terms are suppressed. In the right panel of Fig. 4 we demonstrate the plateaus for the derivative summation method, fitting to a constant to extract the matrix element of the ground state. Within statistical accuracy all three momenta are flat within errors, and are thus described well by a constant.

In Fig. 5 we show the results extracted using two-state fits for both electric and magnetic form factors. The data correspond to the ratio of Eq. (9) and the curves are obtained by fitting simultaneously the three- and two-point functions to Eqs. (14) and (13). The gray horizontal band shows the nucleon matrix element value and error extracted from the two-state fit as in Eq. (15). For the electric form factor, the ratio shows a trend towards lower values as we increase the sink-source separation, with t_s/a=20 becoming compatible with the value extracted from the two-state fit. In the case of the magnetic form factor, the value extracted from the two-state fit is compatible with the ratio for all time separations considered confirming the weak dependence of the matrix element on the sink-source time separation observed in the plateau method.

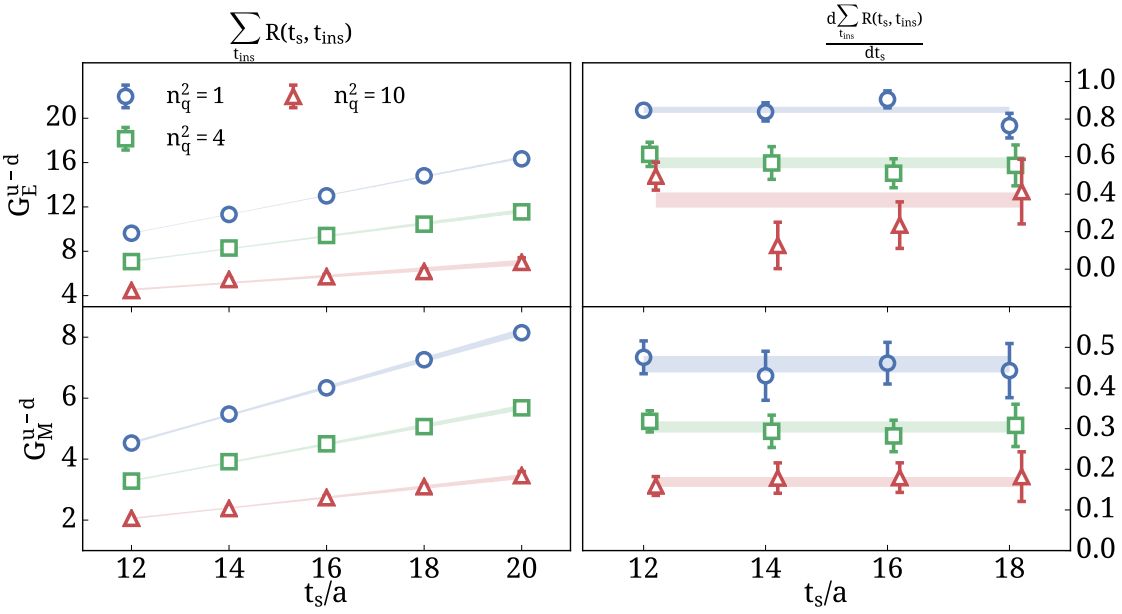

FIG. 4. Left panel: the summed ratio of Eq. (16) as a function of the sink-source time separation for three momenta, namely n_q^2=1 (blue circles), n_q^2=4 (green squares) and n_q^2=10 (red triangles) corresponding to Q^2=0.056, 0.216, and 0.547 GeV^2 for the isovector electric (top) and isovector magnetic (bottom) form factors. The bands are fits to a linear form. Right panel: the derivative of the summed ratio as in Eq. (17), using the same notation as that of the left panel. The bands are fits to a constant.

In Fig. 6 we show the extracted values for the matrix element yielding the isovector electromagnetic form factors. We compare the plateau, summation, derivative summation and two-state fit methods. For the plateau method we show the value extracted from the constant fit for all sink-source separations available. For the other cases we vary the lower fit range, keeping the upper range fixed to t_s/a=20. We seek for the earliest agreement between the plateau method and the other three cases. As already pointed out, the isovector electric form factor shows more severe excited state effects for large Q^2-values and we therefore take the largest time separation

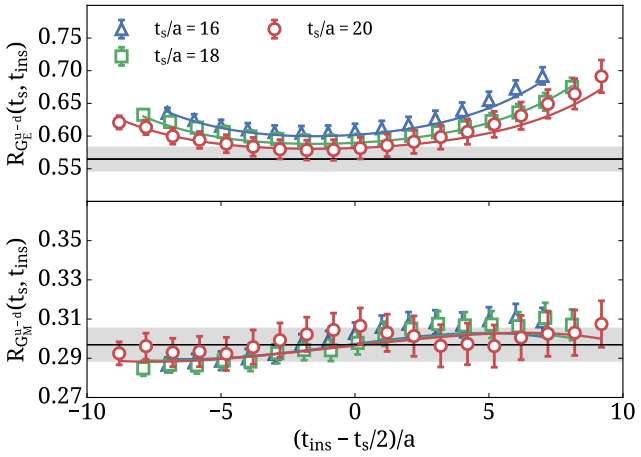

FIG. 5. Ratio yielding the isovector electric (top) and the isovector magnetic (bottom) form factors, for the three largest sink-source separations, following the notation of Fig. 2. The curves show the result of the two-state fit method, while the gray horizontal band is the extracted value of the nucleon matrix elements and its error. We show the case for Q^2=0.216 GeV^2.

for the plateau method to fulfill our criterion for agreement with the other methods. For the isovector magnetic form factor, although excited state effects are mild, we still observe a shift to larger values for the smallest Q^2 and, therefore, we conservatively use the largest time separation available also in this case. An additional observation is that summation and derivative summation methods produce compatible results with similar accuracy, as can be seen in Fig. 6, and thus from now on we will restrict to showing results only from the summation method.

In Fig. 7, we present our results for $G_E^{u-d}(Q^2)$ and $G_M^{u-d}(Q^2)$ as a function of the momentum transfer squared Q^2. We show up to Q^2=0.5 GeV^2 to facilitate comparing the values extracted using the plateau at the four largest separations, the summation, and the two-state fit approaches. The summation and two-state fit are obtained using the fit ranges indicated by the open symbols in Fig. 6. As can be seen, the results follow the observation made in Fig. 2, namely that for the electric form factor effects of excited states are small for small values of Q^2 but become more severe for higher Q^2 values, with the extracted value decreasing with increasing time separation. For $G_M^{u-d}(Q^2)$, excited state effects are small for larger Q^2 values whereas for smaller Q^2 values there is an increase in the values of the form factor with the time separation.

For the extraction of the connected isoscalar form factors we follow a similar procedure as in the isovector case. In Fig. 8 we present the connected contribution to isoscalar electric and magnetic form factors comparing the plateau, summation and two-state fit methods. Excited states have a smaller effect on the isoscalar form factors being detectable only for the magnetic at small values of Q^2 where the two-state fit yields systematically larger values. In what follows, we will consider the plateau values for the largest time separation as the final results on the form factors. We will use the deviation from the values determined from the two-states fits as an estimate of the systematic error due to excited states.

B. Assessment of finite volume and unquenching effects

For the assessment of finite volume effects we compare two N_f=2 physical point ensembles with $m_\pi L \simeq 3$ [7] and $m_\pi L \simeq 4$. The lattice spacing and pion mass are the same for the these two ensembles. The isovector electric and magnetic form factors are shown in Fig. 9, where results are extracted using the plateau method. The results fall, within errors, on the same curve indicating no significant finite volume effects between the two volumes available to us, namely $m_\pi L \simeq 3$ and $m_\pi L \simeq 4$. The same behavior is observed for the isoscalar form factors shown in Fig. 10.

To check for unquenching effects, we compare the N_f=2 ensemble with $m_\pi L \simeq 3$ to the N_f=2+1+1 ensemble. From this comparison, we see that both isovector, shown in Fig. 11, and isoscalar, shown in Fig. 12, show no sensitivity to quenching effects of the strange and charm quarks, at least to the accuracy of our data.

C. Disconnected contributions

A major component of this work is the evaluation of the disconnected contributions shown diagrammatically in Fig. 1 that enter in the evaluation of the isoscalar as well as in the proton and neutron form factors.

The disconnected quark loops are computed using the formalism described in Section III B with the statistics summarized in Table III. As already discussed, the hierarchical probing method, combined with deflation of the low eigenmodes, provides an accurate determination of the diagonal of the quark propagator entering in the evaluation of the quark loops. It is thus preferable to use the local vector current for the evaluation of the disconnected contributions since the conserved current includes non-diagonal terms. We therefore need the renormalization function Z_V, which is determined non-perturbatively, in the RI′-MOM scheme, employing momentum sources. We perform a perturbative subtraction of $\mathcal{O}(g^2a^\infty)$-terms, as described in Refs. [41, 42], which subtracts the leading cut-off effects leaving only a weak dependence on the renormalization scale $(a\mu)^2$, as shown in Fig. 13. We find a value of Z_V=0.728(1) where the error is statistical. Alternatively, Z_V can be determined at $Q^2 = 0$, by taking the ratio of $G_E^{u-d}(0)$ computed with the unrenormalized local current to $G_E^{u-d}(0)$ computed using the lattice conserved current. The ratio yields a value of 0.715(3), which, although 2% smaller than Z_V

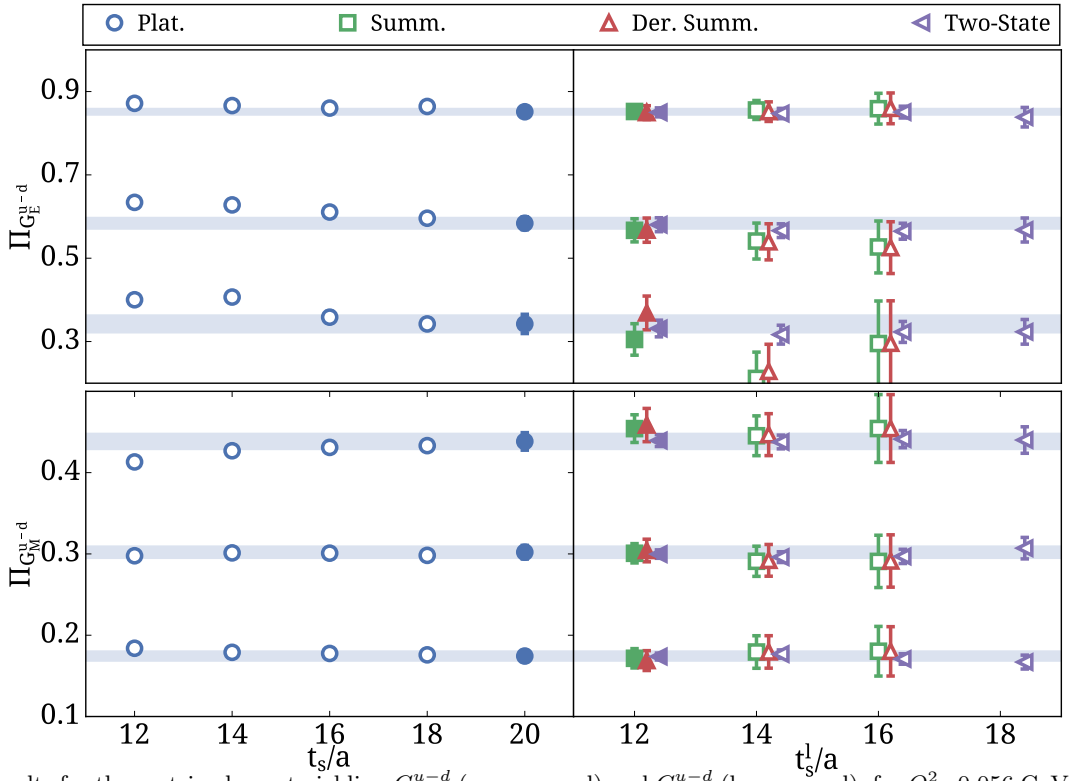

FIG. 6. Results for the matrix element yielding G_E^{u-d} (upper panel) and G_M^{u-d} (lower panel), for Q^2=0.056 GeV, Q^2=0.216 GeV and Q^2=0.547 GeV^2 from top to bottom. In the left column we show the extracted values using the plateau method (blue circles) for all five separations analyzed, while in the right panel we show the values extracted using the summation (green squares), derivative summation (red upper triangles) and two-state fit (purple left triangles) approaches as we change the lower fit range keeping the upper fit range fixed to t_s/a=20. The filled circle and band show the value and statistical error used to quote our final result, while the other filled symbols show the fit ranges for the two-state fit and summation methods that will be used in the figures that follow.

as determined from the vertex function, the difference between them is still an order of magnitude smaller as compared to the statistical errors for the disconnected contributions. In what follows we use Z_V=0.728(1) to renormalize the matrix elements computed using the local current, since this determination has taken into account higher order cut-off effects as compared to the one determined from the ratio. We note that Z_V is only enters in the disconnected three-point function. A more detailed description of the renormalization procedure including other renormalization functions will be provided in a future publication.

Disconnected quark loops are evaluated for every time-slice allowing us to compute the three-point function for every combination of t_s and $t_{\rm ins}$. As in the case of the connected, we are seeking for a reasonable window in t_s to extract the nucleon matrix elements, where excited states are sufficiently suppressed and noise is not prohibitively large. In contrast to the connected diagram, where we have results only for the case $\vec{p}'$=$\vec{0}$, for the disconnected diagrams we have all sink momenta at no additional cost. We analyze, besides $\vec{p}'$=$\vec{0}$, the matrix element for the six final momenta with $\vec{p}'=\pm\frac{2\pi}{L}\hat{n}$, with $\hat{n}=\hat{x}$, $\hat{y}$, or $\hat{z}$, i.e. the unit vector in one of the three spatial directions. Given that the statistical errors in the case of the disconnected diagrams are larger as compared to the connected diagrams we restrict ourselves in using the plateau method for different values of t_s in order to check for ground state dominance. Two-state fits yield too large errors and are in general consistent with the plateau extraction.

In Fig. 14 we present our results for the disconnected contributions to $G_E^{u+d}(Q^2)$ and $G_M^{u+d}(Q^2)$ up to Q^2=1 GeV^2 for three time separations in the range 0.97 fm to 1.29 fm. As can be seen we can achieve a relative statistical error that is less than 20% for up to t_s=14a∼1.15 fm, which is unprecedented given that we are using a physical pion mass ensemble. As we increase the time separation from t_s/a=12 to t_s/a=14 we observe, for both $G_E^{u+d}(Q^2)$ and $G_M^{u+d}(Q^2)$, that the absolute value tends to increase. The results extracted for t_s/a=16 are in a very good agreement with those extracted for $t_a = 14a$ for most Q^2 values, albeit with much larger errors. We therefore take as our final result for the disconnected contribution the value extracted using t_s/a=14 for both $G_E^{u+d}(Q^2)$ and $G_M^{u+d}(Q^2)$. We use the difference between the central value of the results at $t_s = 14a$ and $t_s = 16a$ as an estimate of the systematic error from excited state ef-

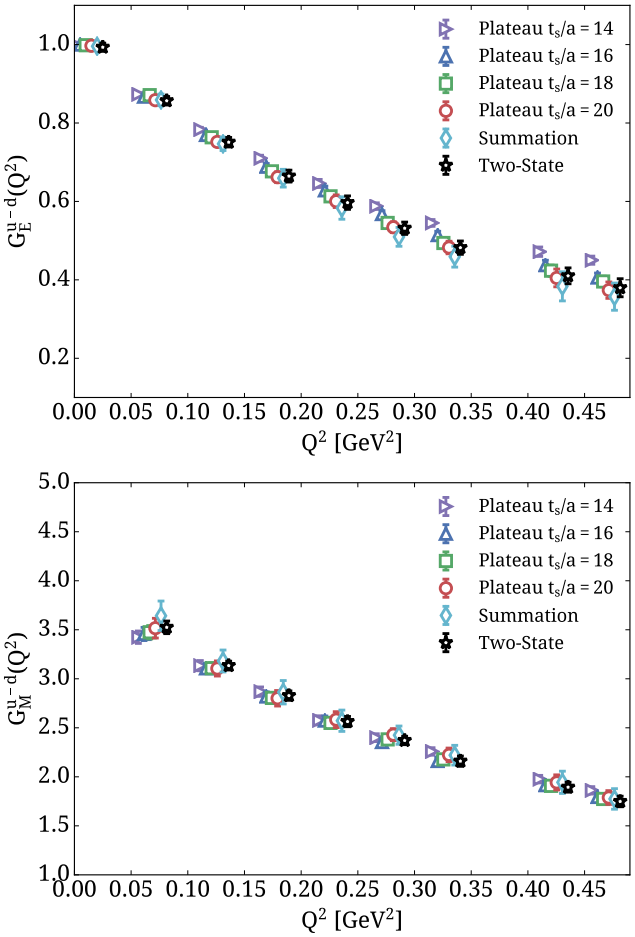

FIG. 7. The isovector electric (upper panel) and magnetic (lower panel) form factor as a function of Q^2. We show the values extracted from fitting the plateau for the four largest t_s values, namely t_s/a=14 (right triangles), t_s/a=16 (triangles), t_s/a=18 (squares) and t_s/a=20 (circles), compared to the summation method (diamonds) and using two-state fits (stars). Results from different methods are slightly shifted to the right for clarity.

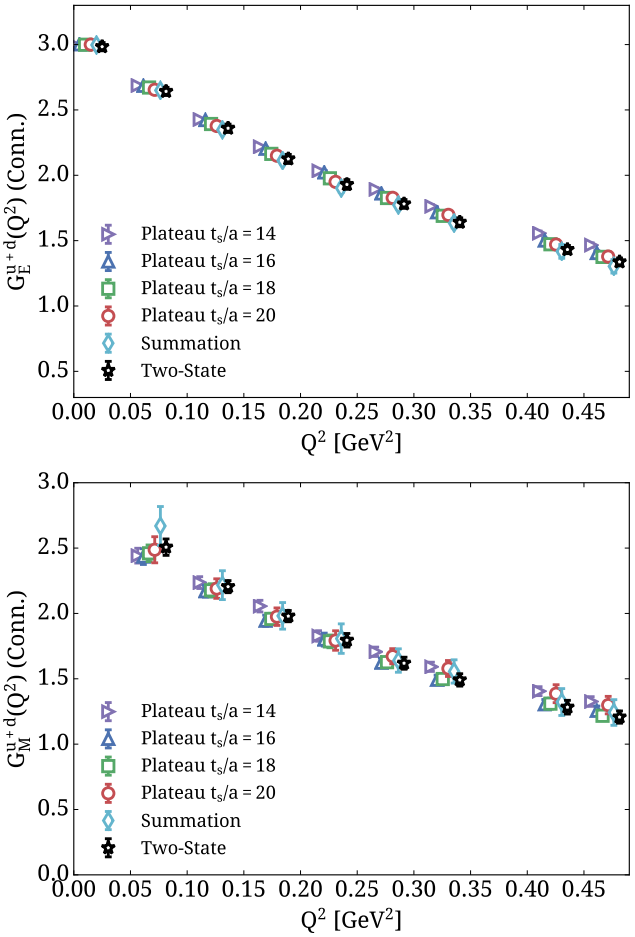

FIG. 8. Connected contribution to the isoscalar electric (upper panel) and magnetic (lower panel) form factor. The notation is the same as in Fig. 7.

fects when we quote quantities that include disconnected contributions.

In Fig. 15 we show the disconnected contributions to G_E^{u+d} and G_M^{u+d} comparing between results obtained using the $N_f = 2+1+1$ and $N_f = 2$ with $Lm_\pi \sim 3$ twisted mass ensembles. As can be seen, the values are consistent but the N_f=2+1+1 results have up to four times smaller statistical errors. In evaluation of the disconnected contributions of the $N_f = 2$ ensemble we used 2120 configurations with 100 source positions for the computation of the two-point functions and 2250 stochastic vectors for the disconnected loops [6]. This is approximately the same number of inversions (and thus cost) as for the N_f=2+1+1 ensemble (see Table III), which demonstrates the effectiveness of the hierarchical probing method employed in the current analysis of the N_f=2+1+1 ensemble [6].

V. Q^2-DEPENDENCE OF THE ISOVECTOR AND ISOSCALAR FORM FACTORS

In this section we fit the Q^2-dependence of form factors to the forms introduced in Section III D. We consider first the isovector form factors where only the connected diagram contributes. In Figs. 16 and 17 we show fits using the dipole form, comparing between results from the plateau method at $t_s/a = 20$ and from two-state fits for $G_E^{u-d}(Q^2)$ and $G_M^{u-d}(Q^2)$, respectively. As can be seen, the values extracted from the plateau and two-state fits are consistent and do not show any systematic effect on the determination of the Q^2-dependence of the form factors, indicating that excited states are sufficiently suppressed. Since results are in agreement, from now on we will use the plateau method at $t_s/a = 20$ to extract final results on the form factors, r.m.s radii, and magnetic moment. We will use the results extracted from the two-state fits to estimate the systematic error due to excited states.

In Figs. 18 and 19, we show fits to $G_E^{u-d}(Q^2)$ and

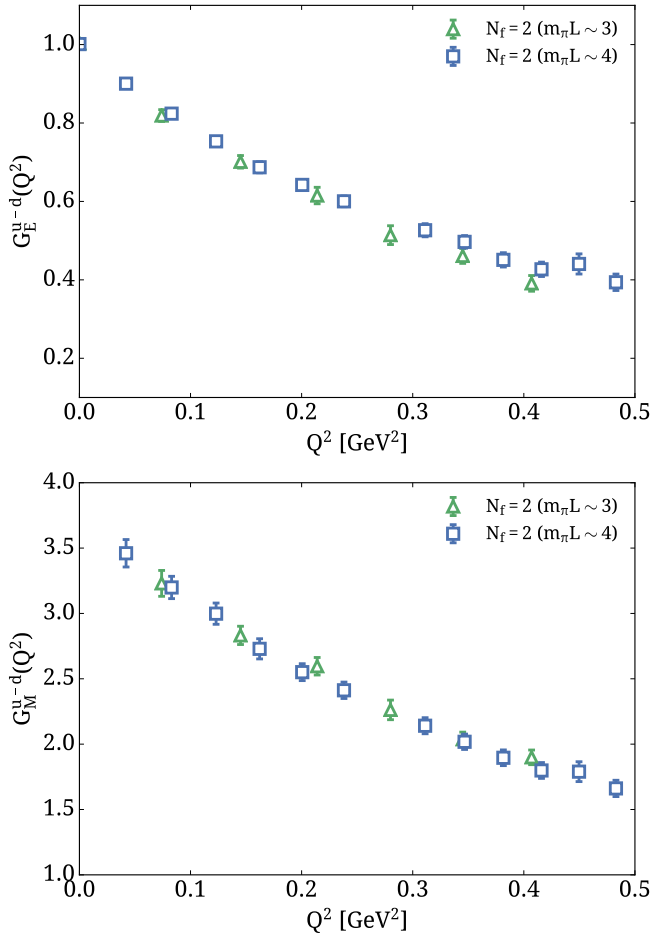

FIG. 9. The isovector electric (top panel) and magnetic (lower panel) form factor for two different physical spatial volumes. With green triangles we show the results for the N_f=2 ensemble and $m_\pi L \simeq 3$ [7] and with blue squares the N_f=2 ensemble with $m_\pi L \simeq 4$. Results are extracted using the plateau method for sink-source separation $t_s \simeq 1.5$ fm for the electric and $t_s \simeq 1.3$ fm for the magnetic form factors.

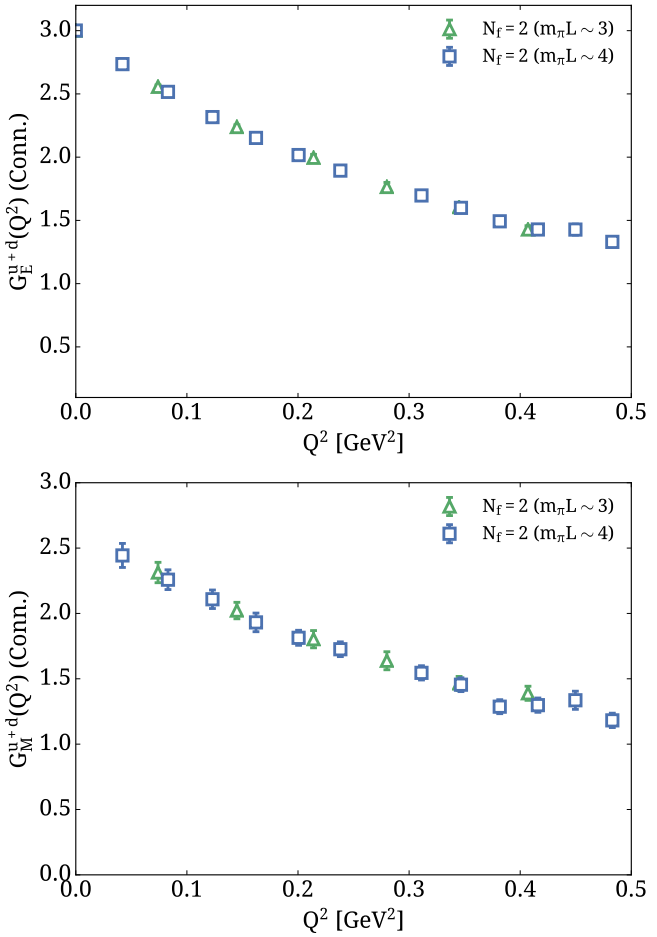

FIG. 10. The isoscalar electric (top panel) and magnetic (lower panel) form factor for two different physical spatial volumes. The notation is as in Fig. 9.

$G_M^{u-d}(Q^2)$, respectively using the dipole form and the z-expansion of Eq. (22) and comparing to experiment. For the z-expansion, we check convergence by increasing $k_{\rm max}$ and observing the resulting magnetic moment and r.m.s radii, shown in Fig. 20, where we observe convergence for $k_{\rm max}$=4. In the case of $G_E^{u-d}(Q^2)$, we see from Fig. 18 that, while our results are compatible with the experimental results for $Q^2 < 0.1$ GeV^2, in the range 0.1-0.6 GeV^2 they are consistently higher. Therefore, although both dipole form and z-expansion describe very well our data, shown in separate panels for clarity, they lie about one to two standard deviations above the experimental values. In extracting the r.m.s radius, we see from Fig. 20 that results obtained from using the dipole fit and z-expansion are compatible, and yield

$$\sqrt{\langle r_E^2 \rangle^{u-d}} = 0.802(19)(12)(1) \text{ fm}, \qquad (25)$$

where the central value and the statistical error are taken from the dipole fit, the second error is a systematic computed as the difference in the mean values between dipole and z-expansion for $k_{\rm max}$=4 and the third error is the systematic error due to excited states obtained from the difference when fitting the form factor extracted from the plateau and from the two-state fit method. Subsequent quantities given in the paper will have statistical and systematic errors quoted using the same convention as in Eq. 25.

For G_M^{u-d}, shown in Fig. 19, we observe that our results are in agreement with the experimental values for $Q^2 > 0.15$ GeV^2, whereas for small Q^2 they tend to be lower. A possible explanation for this discrepancy is that effects from the pion cloud, expected to be prominent for small momenta [57], are suppressed in our calculation due to our finite volume. The fact that we have seen no volume effects when we increase the volume from $Lm_\pi \simeq 3$ to $Lm_\pi \simeq 4$ for our two $N_f = 2$ ensembles may indicate that pion cloud suppression may not be detectable for these volume sizes requiring larger volumes to unfold. Indeed, preliminary results by PACS using a physical point ensemble with $Lm_\pi \simeq 7.4$ [58] finds a higher value that may

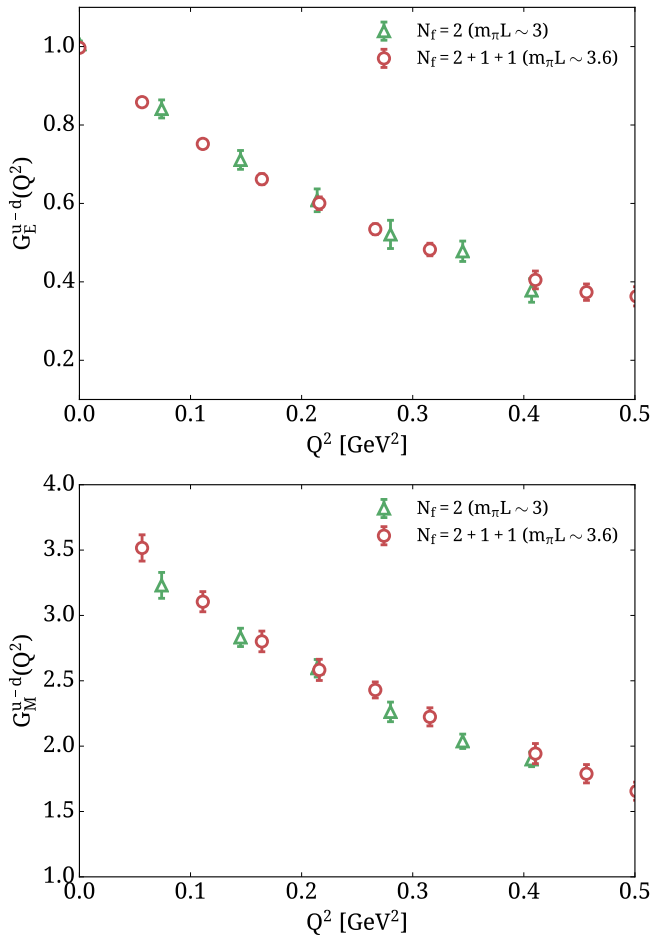

FIG. 11. Comparison of the isovector electric (top panel) and magnetic (lower panel) form factors between N_f=2 [7] (green triangles) and N_f=2+1+1 (red circles). Results are extracted using the plateau method for sink-source separation $t_s \simeq 1.6$ fm for the N_f=2+1+1 and for the electric for the N_f=2 while for the magnetic N_f=2 the separation is $t_s \simeq 1.3$ fm.

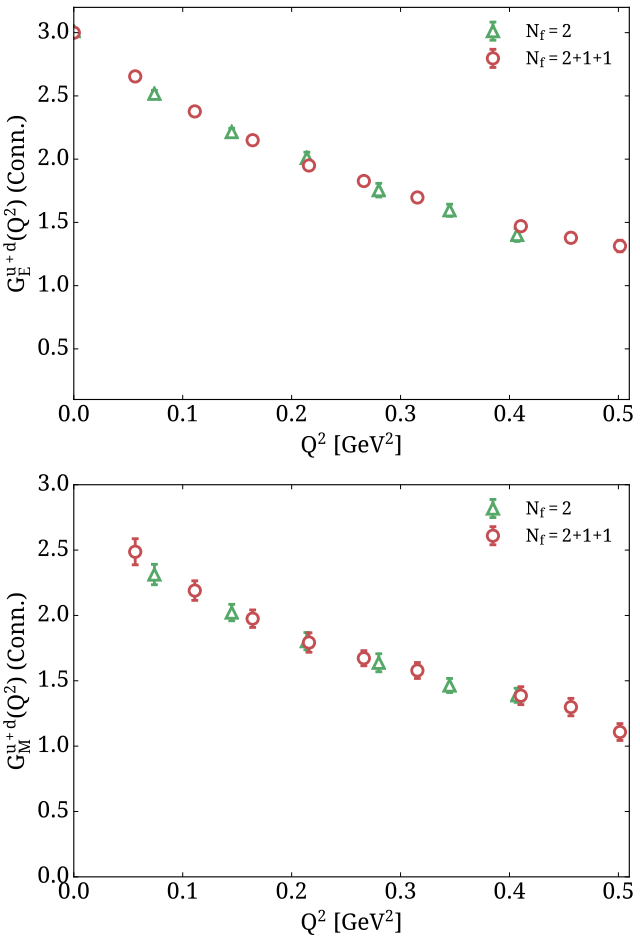

FIG. 12. Comparison of the connected contribution to the isoscalar electric (top panel) and magnetic (lower panel) form factors between N_f=2 [7] and N_f=2+1+1 wit the same notation as in Fig. 11.

point to a finite volume effect. This would need further investigation to confirm.

The isovector magnetic moment and mean square magnetic radii are shown in Fig. 20. As can be seen, the mean value extracted for μ^{u-d} using the dipole and z-expansion is the same, while for $\langle r_M^2 \rangle^{u-d}$ the z-expansion produces a slightly higher value, which however is consistent within errors. Using the dipole fit we find

$$\mu^{u-d} = 3.96(14)(3)(7)\binom{1}{0} \tag{26}$$

$$\sqrt{\langle r_M^2 \rangle^{u-d}} = 0.714(26)(88)(16)\binom{1}{0}\ \text{fm}\,. \tag{27}$$

Here we have included a fourth systematic error computed as the difference in the values of μ^{u-d} and $\langle r_M^2 \rangle^{u-d}$ when fitting $G_M^{u-d}(Q^2)$ including and excluding the lowest Q^2 value from the fit. The error is asymmetric, since the expectation is that pion cloud effects will increase the value of the magnetic form factor. It is also small compared to the systematic error due to excited states. In what follows we will not include this fourth systematic error.

Before presenting fits to the total isoscalar form factors we discuss the Q^2-dependence of the disconnected contributions. In Fig. 21 we show the disconnected contribution to the isoscalar electric form factor G_E^{u+d}, accompanied by fits to the Galster-like parameterization and z-expansion. We note that in the case of the z-expansion we take a_0=0, since $G_E^{u+d}(0)$=0 for the disconnected contribution. Although both parameterizations describe well our results, we observe different behavior in the errors, namely the z-expansion has a larger error band for larger Q^2 values.

The disconnected contribution to $G_M^{u+d}(Q^2)$ is shown in Fig. 22. We find that both dipole and z-expansion are in good agreement. In particular, they yield compatible values at zero momentum transfer. Like in the case of the disconnected contribution to $G_E^{u+d}(Q^2)$, for large Q^2 the dipole fit has a smaller error band as compared to the z-expansion. The values extracted from fitting the

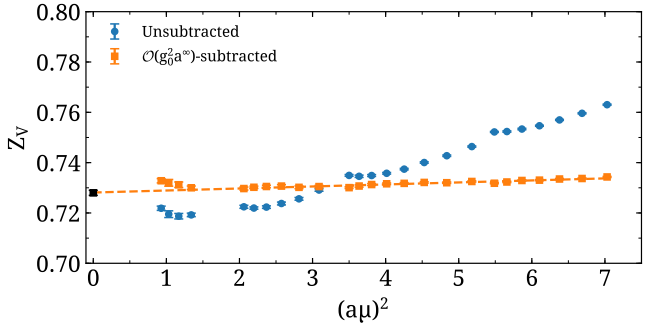

FIG. 13. The renormalization constant Z_V as a function of the renormalization scale squared $(a\mu)^2$ before (blue circles) and after (orange squares) performing the subtraction of $\mathcal{O}(g^2a^\infty)$-terms. The dashed line is a linear fit to the latter and the point at $(a\mu)^2 = 0$ (black square) is the result of the fit.

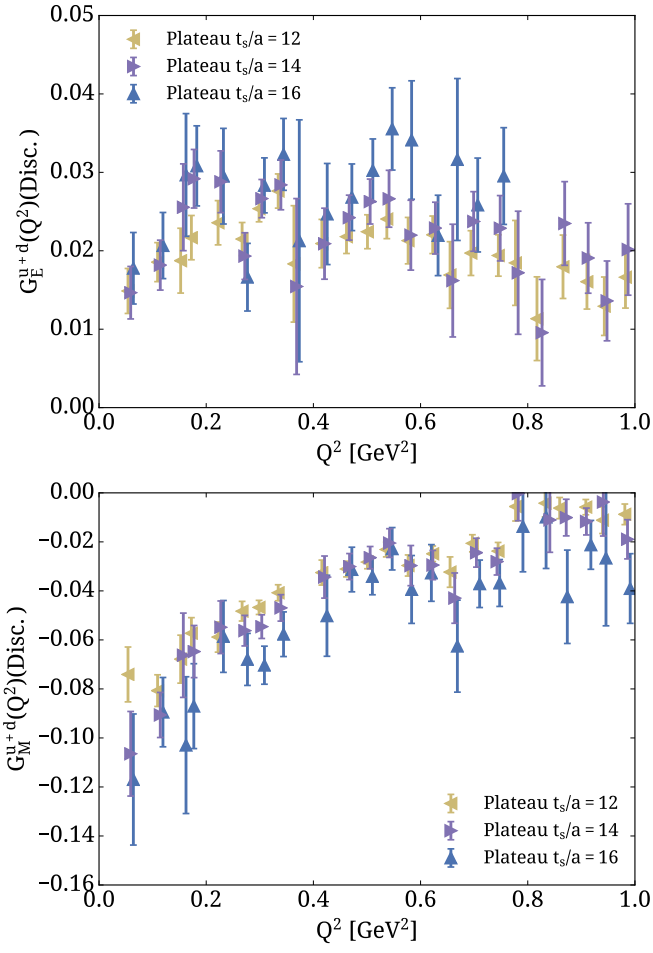

FIG. 14. The disconnected contributions to G_E^{u+d} (top) and G_M^{u+d} (bottom) using the plateau method for t_s/a=12 (left triangles), t_s/a=14 (right triangles) and t_s/a=16 (upright triangles). Points from closely spaced Q^2 have been averaged for demonstration, and results from different time separations have been slightly shifted to the right for clarity.

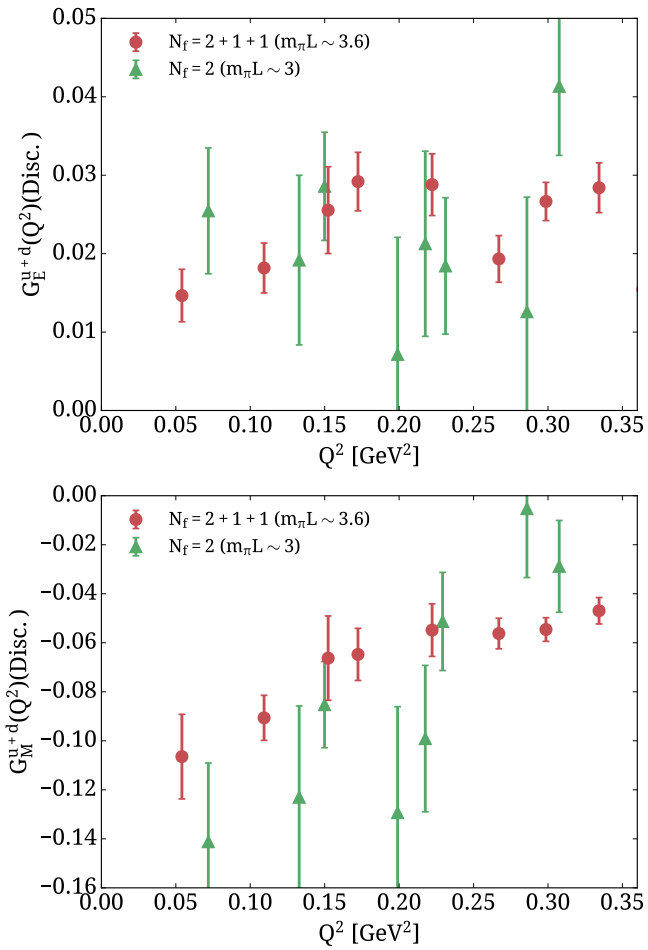

FIG. 15. Disconnected contributions to G_E^{u+d} (top) and G_M^{u+d} (bottom) from the N_f=2+1+1 ensemble of this work using t_s/a = 14 (circles) compared to the N_f=2 results of Ref. [6] (triangles).

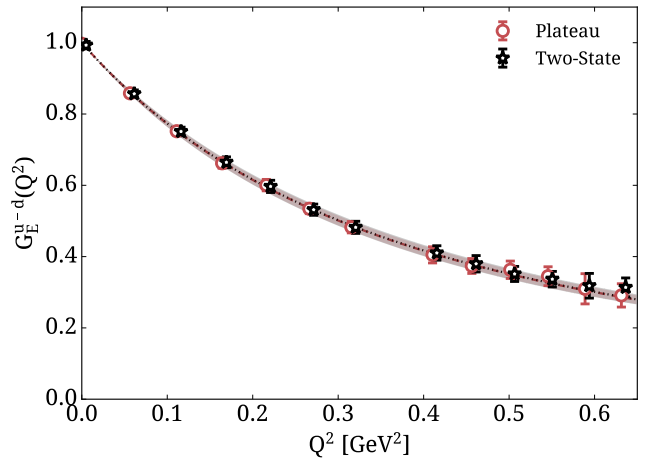

FIG. 16. $G_E^{u-d}(Q^2)$ from the plateau method for t_s/a = 20 (circles) and two-state fits (stars). The dashed (dotted) curve and corresponding band is a dipole fit to the plateau (two-state) fit results, which overlap.

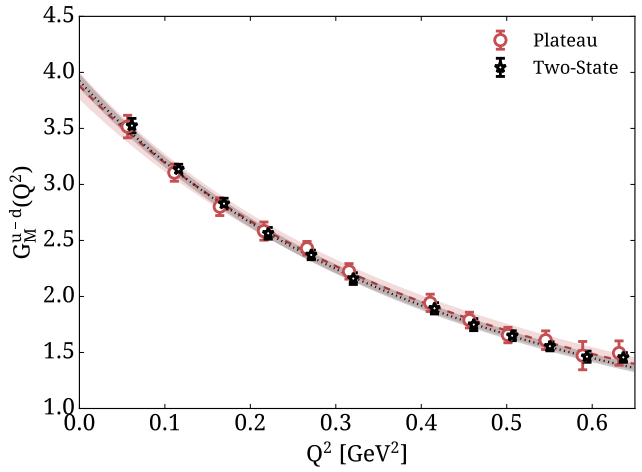

FIG. 17. $G_M^{u-d}(Q^2)$ from the plateau method for $t_s/a = 20$ (circles) and two-state fits (stars). The rest of the notation is as in Fig. 16.

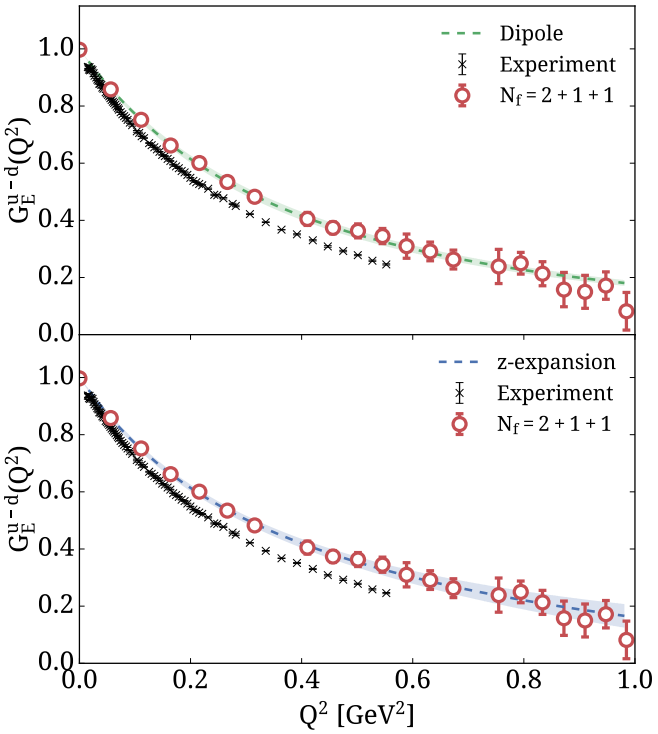

FIG. 18. The isovector electric form factor as a function of Q^2 (circles). We show fits to our results using a dipole form (top) and using the z-expansion (bottom) for $k_{\max}$=4. Black crosses are experimental results taken from the A1 collaboration [1] for the proton and from Refs. [4, 43–56] for the neutron.

disconnected contributions alone are

$$\langle r_E^2\rangle^{u+d}(\text{Disc.}) = -0.072(6)(4)(6)\ \text{fm}^2, \quad (28)$$
$$\mu^{u+d}(\text{Disc.}) = -0.135(17)(1)(10), \quad (29)$$
$$\langle r_M^2\rangle^{u+d}(\text{Disc.}) = -0.137(30)(2)(12)\ \text{fm}^2, \quad (30)$$

where we have not normalized with the value of the form factor at zero momentum transfer, i.e. the radii are extracted from $\langle r^2\rangle = -6\frac{\partial G(q^2)}{\partial q^2}\Big|_{q^2=0}$ rather than from Eq. 5.

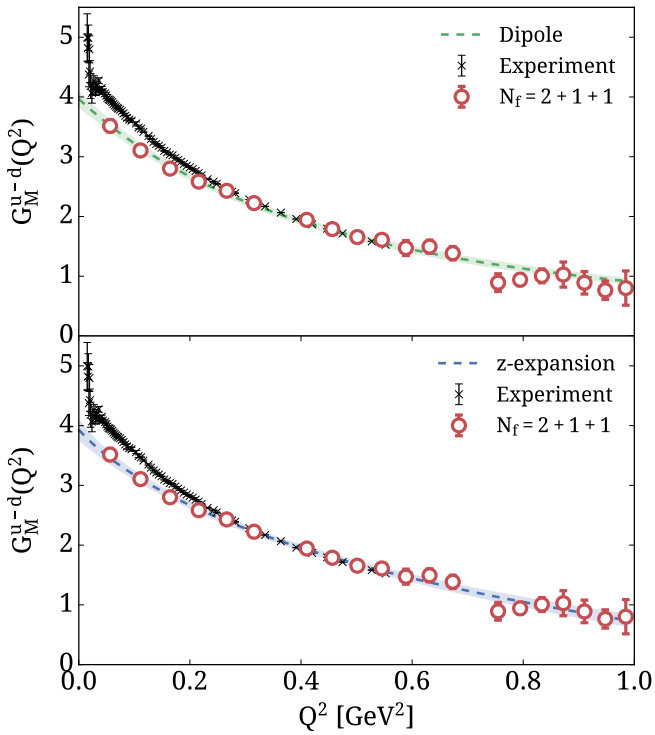

FIG. 19. The isovector magnetic form factor fitted using a dipole form (top) and using the z-expansion (bottom) with the notation of Fig. 18.

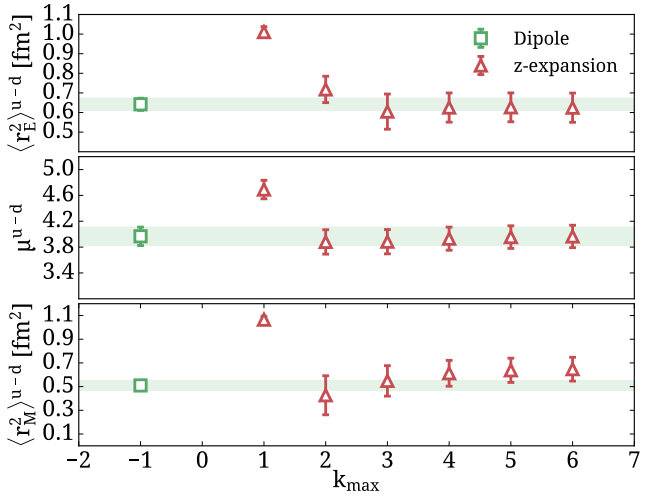

FIG. 20. Results for the isovector charge radius $\langle r_E^2\rangle^{u-d}$, magnetic moment μ^{u-d} and magnetic radius $\langle r_M^2\rangle^{u-d}$ from the plateau method using t_s/a=20 as extracted from a dipole fit (green square) and z-expansion (red triangles). The latter are shown as a function of $k_{\max}$. The green band is the statistical error on the value extracted from the dipole fit.

In Fig. 23 we compare results between including and excluding disconnected contributions. Although the effect is small for both $G_E^{u+d}(Q^2)$ and $G_M^{u+d}(Q^2)$ there is a shift in the fits affecting the parameters of the fits.

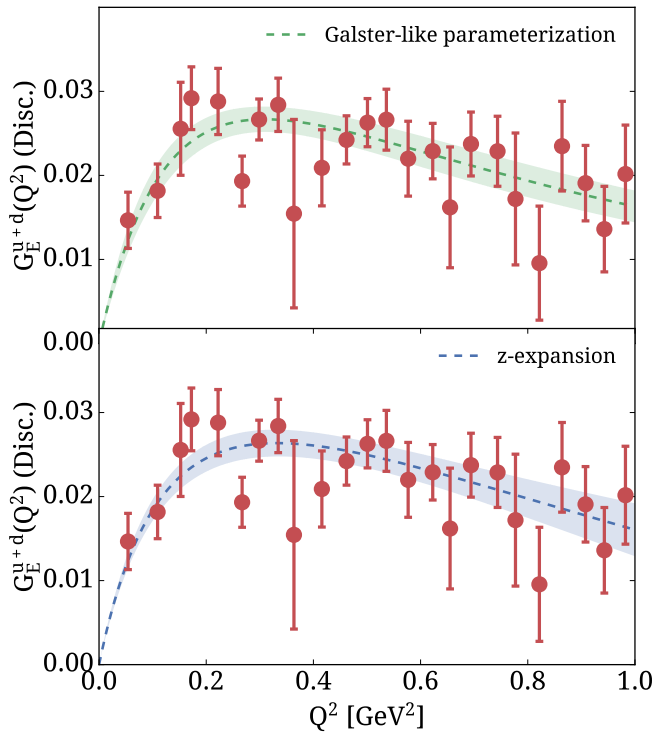

FIG. 21. Disconnected contributions to the isoscalar electric form factor (circles) as a function of Q^2. The fits using the Galster-like parameterization of Eq. (20) and the z-expansion for $k_{\rm max}$=3 are shown in the upper and lower panels, respectively.

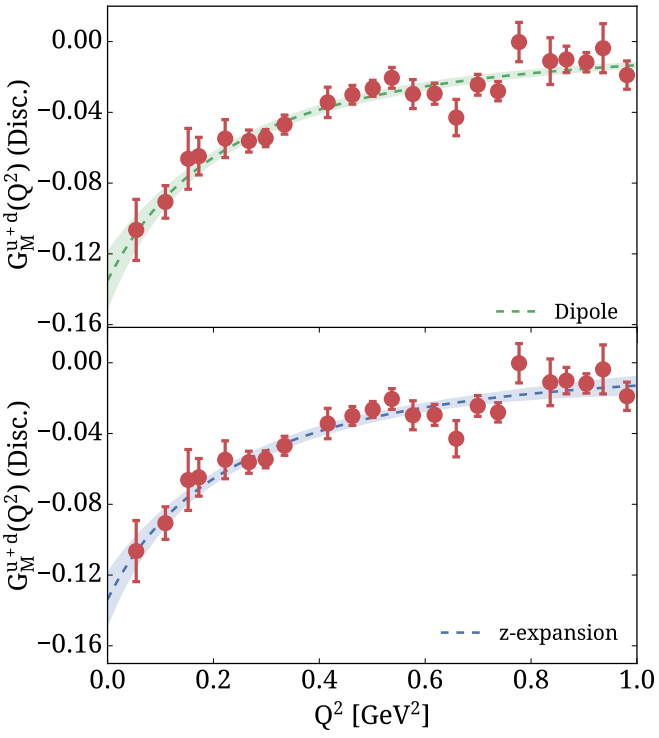

FIG. 22. Disconnected contributions to the isoscalar magnetic form factor. The notation is the same as in Fig. 21.

This comparison shows that disconnected contributions are thus non-negligible and that their omission would result in an uncontrolled systematic error comparable to the statistical uncertainty. Such systematics need to be under control for precision results required for distinguishing e.g. the two experimental determinations of the charge radius of the proton.

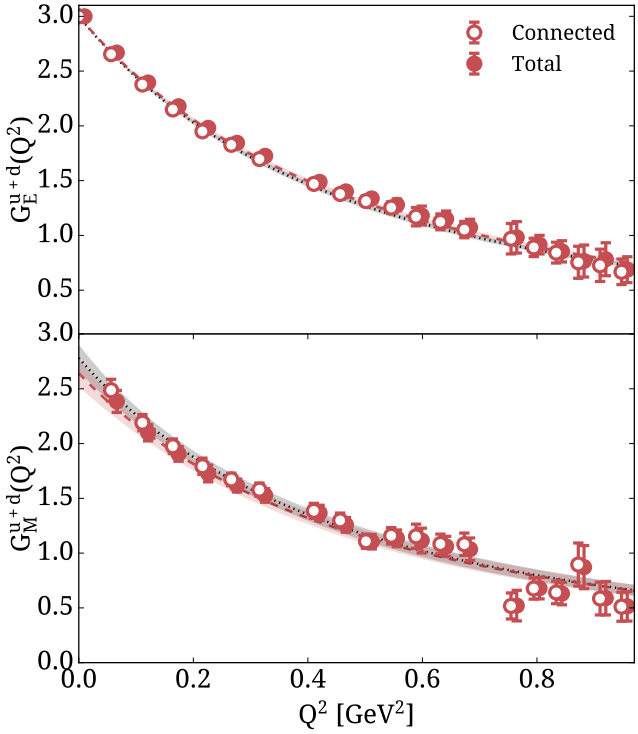

FIG. 23. Comparison of the connected (open circles) and total (filled circles) contributions to the isoscalar electric (top) and magnetic (bottom) form factors. Dipole fits to the connected and total contributions are shown with the dotted and dashed curves respectively.

In Figs. 24 and 25 we show the fits of the total isoscalar electric and magnetic form factors using the dipole form and z-expansion. Both fits describe well the data with the dipole fit being more precise at larger Q^2, a behavior also observed for the isovector form factors. For intermediate Q^2 values our results are systematically higher by one to two standard deviations compared to experiment, which is then reflected in the fit bands. Since for low Q^2 there is agreement, the extracted value for the isoscalar magnetic moment agrees with the experimental value. On the other hand, the slope of our lattice data is not as steep as in the experimental results, which leads to a smaller value for the corresponding radii.

In the top panel of Fig. 26 we show the isoscalar electric square radius. As can be seen, the z-expansion fit yields values that are within errors for $k_{\rm max} > 1$ but with two times larger errors than the dipole. In Fig. 26 we also show results for the magnetic moment and the magnetic radius where convergence of the z-expansion is observed already for $k_{\rm max}$=2. For the magnetic moment,

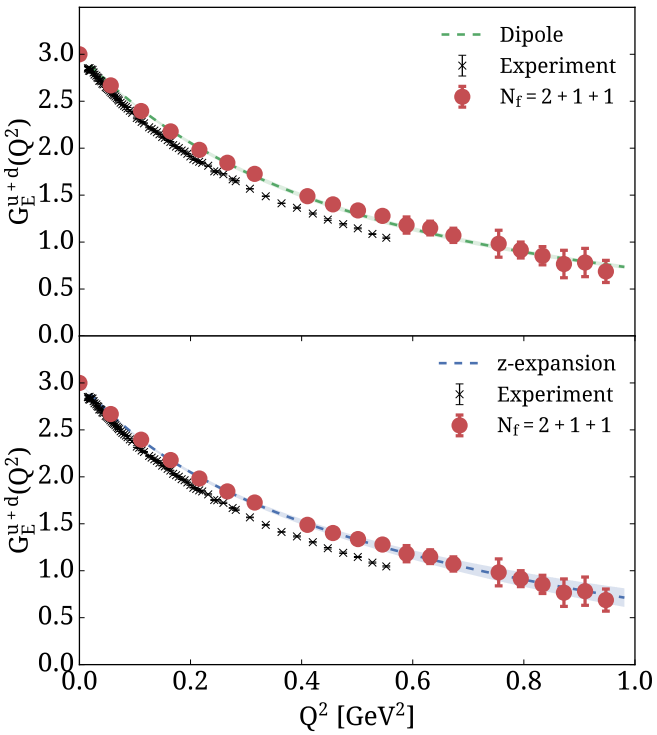

FIG. 24. Isoscalar electric form factor (circles) as a function of Q^2. We combine the connected contribution from the plateau for t_s/a=20 with the disconnected contribution for t_s/a=14. The remaining notation is as in Fig. 18.

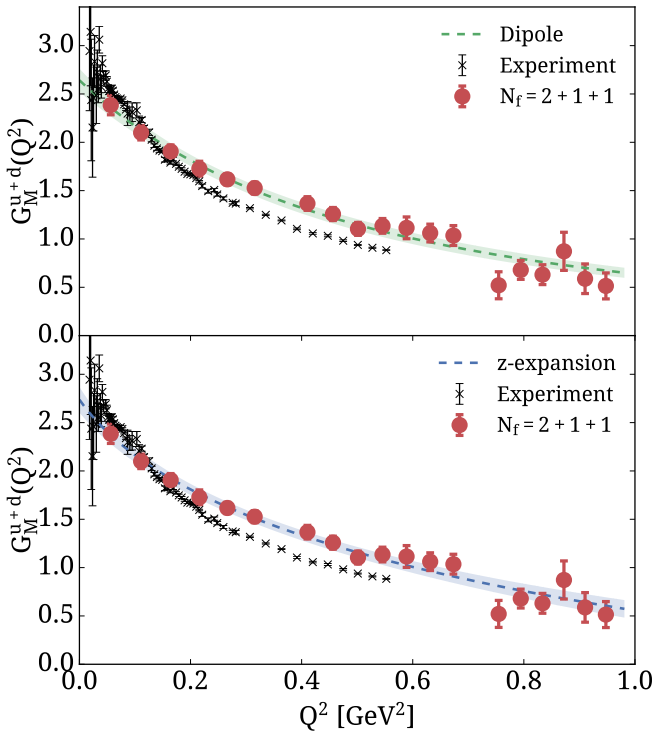

FIG. 25. Isoscalar magnetic form factor. The notation is as in Fig. 24.

dipole and z-expansion are compatible with similar errors while for the magnetic radius the z-expansion tends to be slightly higher but with bigger errors. In what follows we will quote the values determined from the dipole fits. They are

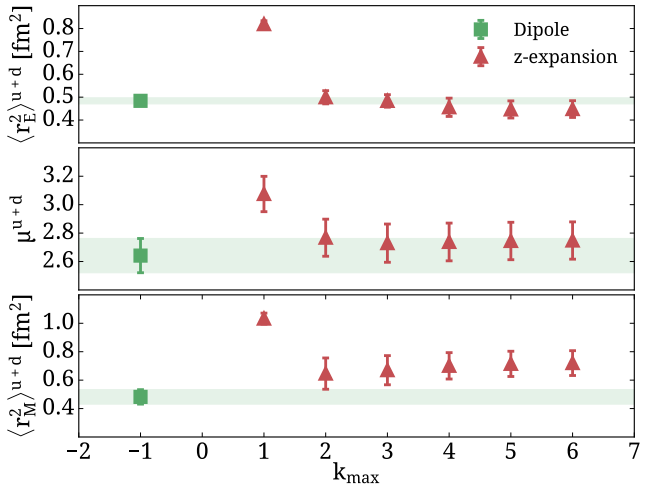

FIG. 26. Results for the isoscalar charge square radius, magnetic moment, and magnetic square radius. The notation is as in Fig. 20.

$$\sqrt{\langle r_E^2\rangle^{u+d}} = 0.697(9)(10)(0)\ \text{fm} \quad (31)$$

$$\mu^{u+d} = 2.64(12)(13)(6) \ \text{ and} \quad (32)$$

$$\sqrt{\langle r_M^2\rangle^{u+d}} = 0.695(37)(108)(3)\ \text{fm}\,. \quad (33)$$

Note that from our definition of the isoscalar combination, the proton plus neutron magnetic moment is obtained by: $\mu^p + \mu^n = \mu^{u+d}/3$.

VI. COMPARISON WITH OTHER STUDIES

Before we discuss our final results for the proton and neutron form factors we compare with results by other groups using different lattice QCD ensembles and discretization schemes. These mainly exist for the isovector electromagnetic form factors allowing us to qualitatively assess lattice artifacts. This is useful since most groups use a single ensemble and thus infinite volume and continuum extrapolations are lacking. We summarize the lattice QCD discretized actions used by different groups for the computation of the electromagnetic form factors, restricting ourselves only to published work and results that were obtained using simulations with pion mass less than 170 MeV:

- LHPC analyzed one ensemble of N_f=2+1 with two levels of HEX-smeared clover fermions with m_π=149 MeV, lattice spacing a=0.116 fm and Lm_π=4.21 at three sink-source separations from 0.93 fm to 1.39 fm [13]. They give as their final results the ones extracted using the summation method, which leads to larger statistical errors.

Additionally, they analyzed an N_f=2+1 ensemble with two levels of HEX-smeared clover fermions with m_π = 135 MeV, lattice spacing a=0.093 fm and Lm_π=4 [14]. They analyzed three lattice separations from 0.93 fm to 1.5 fm and they have extracted results using the summation method. A momentum derivative method has been used to extract the magnetic moment and the electric radius directly from the correlation functions avoiding a fitting procedure.

- The PACS collaboration analyzed an ensemble of N_f=2+1 stout-smeared clover fermions with m_π=146 MeV, $a \simeq 0.085$ fm and a spatial extend of 8.1 fm or $Lm_\pi \simeq 6$ allowing access to relatively small momenta [15]. PACS has computed three-point functions for one sink-source time separation of 1.27 fm and they used the plateau method to identify the ground state matrix element. Recently a followup study from PACS appeared but this work has not yet been published [58].

- Our results obtained using the three ensembles of Table I simulated by the Extended Twisted Mass Collaboration (ETMC). These include the two analyses of this work, namely the N_f=2+1+1 ensemble with m_π=135 MeV, a=0.0809(2)(4) fm and Lm_π ≃3.6 and the N_f=2 ensemble with m_π=130 MeV, a=0.0938(3)(1) fm and $Lm_\pi \simeq 4$ as well as our results from Refs. [6, 7] which used the N_f=2 ensemble with m_π=130 MeV, a=0.0938(3)(1) fm and $Lm_\pi \simeq 3$.

In the top panel of Fig. 27 we show lattice QCD results from the aforementioned analyses for $G_E^{u-d}(Q^2)$ up to Q^2=0.5 GeV^2. As can be seen, ETMC and PACS results, which use similar techniques to identify the nucleon matrix element are in good agreement but systematically higher than the experimental values. LHPC results were obtained using the summation method and thus have larger statistical errors making them compatible with the experimental values. In the lower panel of Fig. 27, we show the corresponding results for $G_M^{u-d}(Q^2)$. The recent ETMC results are the most precise and in good agreement with those obtained from other studies. We note the very good agreement of lattice QCD results and experiment for Q^2>0.2 GeV^2. The underestimation of lattice QCD results compared to experimental values at smaller Q^2 may indicate that a larger spatial volume is required to develop fully the pion contributions. Although our study using two ensembles of $N_f = 2$ showed no detectable volume effects when we increase the spatial extent from 4.5 fm to 6 fm (or equivalently from $Lm_\pi \sim 3$ to $Lm_\pi \sim 4$) the volume dependence could be weak and require a larger volume to manifest itself. The yet unpublished PACS results may indicate such a trend. A conclusion that we can, however, draw from these lattice QCD studies is that the fact that there is agreement among them for both the electric and magnetic form factors when different discretization schemes are employed

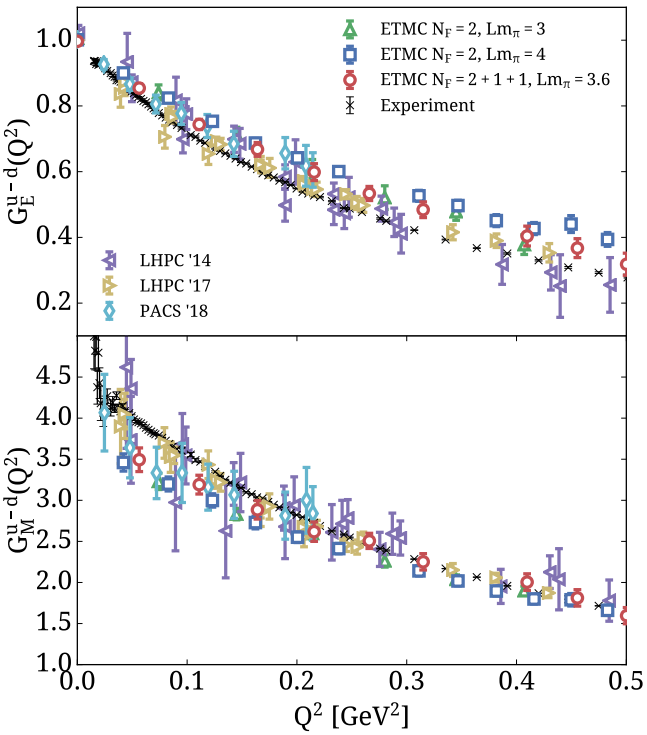

FIG. 27. Comparison of results for $G_E^{u-d}(Q^2)$ (upper panel) and $G_M^{u-d}(Q^2)$ (lower panel) from the N_f=2+1+1 twisted mass ensemble of this work (red circles), the N_f=2 twisted mass ensemble with $m_\pi L \simeq 4$ of this work (blue squares), the N_f=2 twisted mass ensemble with $m_\pi L \simeq 3$ from Ref. [7] (green triangles), LHPC using N_f=2+1 stout-smeared clover fermions from Ref. [13] (left purple triangles) and Ref. [14] (right yellow triangles) and from PACS using N_f=2+1 stout-smeared clover fermions from Ref. [15] (cyan rhombuses).

indicates that cut-off effects are smaller than the statistical errors.

The proton and neutron form factors can be extracted from the isovector and isoscalar form factors discussed in Section V, using the linear combinations

$$G^p(Q^2) = \frac{1}{2}\left[\frac{G^{u+d}(Q^2)}{3} + G^{u-d}(Q^2)\right], \qquad (34)$$

$$G^n(Q^2) = \frac{1}{2}\left[\frac{G^{u+d}(Q^2)}{3} - G^{u-d}(Q^2)\right]. \qquad (35)$$

In Fig. 28, we show lattice QCD results for the proton electromagnetic form factors. To extract these one needs both the isovector and isoscalar combinations. The latter include disconnected contributions, which have only been computed by ETMC at close to physical pion masses. We use filled symbols to indicate lattice results that include disconnected contributions. For both the electric and magnetic form factors our results and those from LHPC are within error bars, with the LHPC results exhibiting larger errors at higher Q^2 possibly due to the use of the summation method. The accurate ETMC results are higher than the experimental values for $G_E^P 0Q^2$) and lower for $G_M^p(Q^2)$ for the two lowest Q^2 values. Although

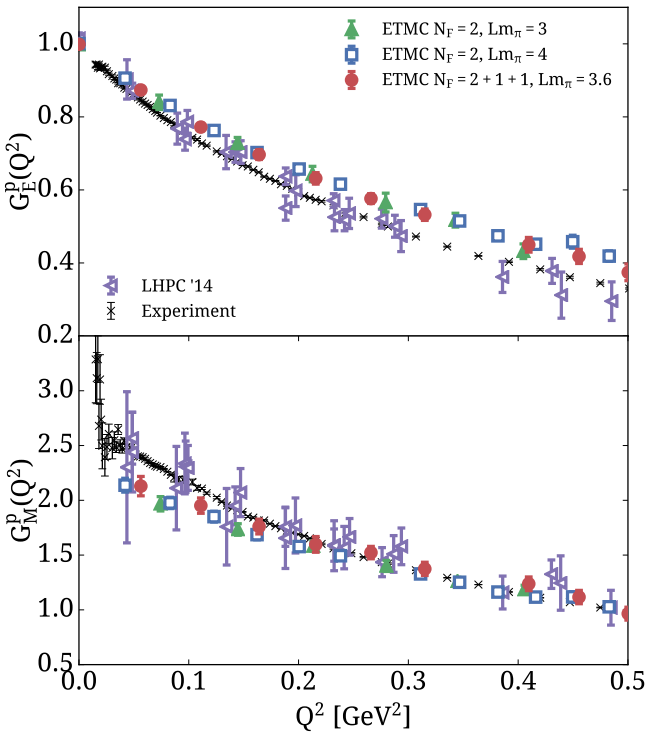

FIG. 28. Comparison of results for $G_E^p(Q^2)$ (upper panel) and $G_M^p(Q^2)$ (lower panel) from ETMC and LHPC following the notation of Fig. 27. Filled symbols are used for results that include disconnected contributions and open symbols for results without disconnected contributions. Black crosses are experimental results from the A1 collaboration [1].

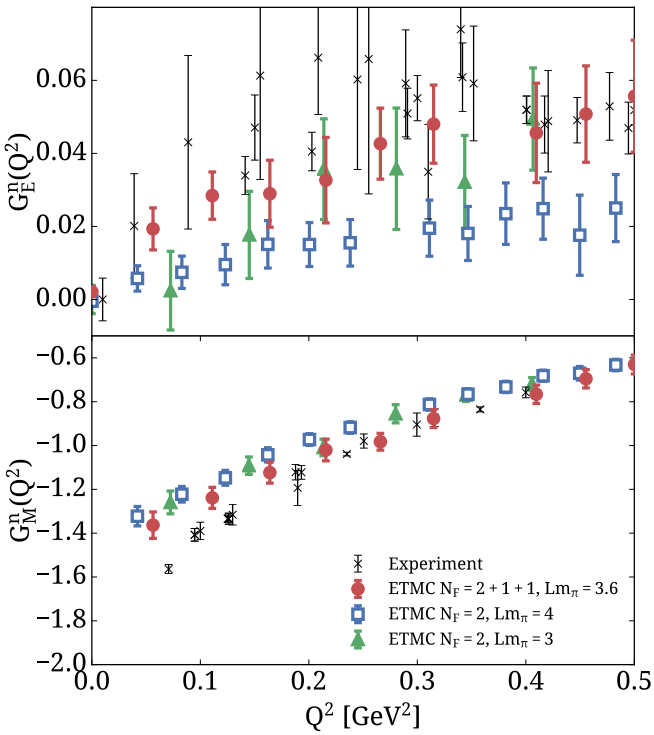

FIG. 29. Comparison of results for $G_E^n(Q^2)$ and $G_M^n(Q^2)$ using the N_f=2+1+1 results of this work (red circles), using the N_f=2 results with $m_\pi L \simeq 4$ of this work (blue squares), and using the N_f=2 ensemble with $m_\pi L \simeq 3$ from Ref. [6] (green triangles). Filled symbols are used for results that include disconnected contributions and open symbols for results without disconnected contributions. Crosses are experimental results taken from Refs. [4, 43–56] for the electric form factor and from Refs. [59–64] for the magnetic form factor.

LHPC results do not show such discrepancies, unfortunately, they carry large errors and thus do not allow for any conclusions to be drawn on the possible reasons for the discrepancy with experiment.

Results for the neutron electromagnetic form factors are only provided by the ETMC for pion masses below 170 MeV. They are compared to the experimental values in Fig. 29. We observe that results for the electric form factor extracted from the N_f=2+1+1 ensemble that include disconnected contributions are in agreement with the experimental values. This is also true for the $N_F = 2$ ensemble with $Lm_\pi \sim 3$ that includes the disconnected contributions although they have larger errors. N_f=2 results, for which disconnected contributions have not been included, underestimate the electric neutron form factor. This clearly indicates the significance of including disconnected contributions, especially for this quantity. For the magnetic form factor, results using the N_f=2+1+1 twisted mass ensemble with disconnected contributions are closer to experiment compared to $N_f = 2$, but there is still a discrepancy with the experiment for small Q^2 that needs to be further investigated.

In Fig. 30, we compare the lattice QCD values of the isovector r.m.s radii $\sqrt{\langle r_E^2\rangle^{u-d}}$, and $\sqrt{\langle r_M^2\rangle^{u-d}}$ finding agreement among them. As expected by the less steep fall-off of the electric isovector form factor, lattice results are systematically lower than the experimental values. We note that the ETMC results have errors that are already the same as the difference between the two experimental determinations showing that the statistical accuracy required can be achieved by increasing statistics. A high-statistics dedicated study to better assess the remaining systematics can thus yield valuable insights on the r.m.s. charge radius from a first principles calculation. In the case of $\langle r_M^2\rangle^{u-d}$ the errors are larger and lattice QCD results are both in good agreement among them and compatible with the PDG value [66].

In Fig. 31 we show the corresponding quantities for the proton. Only the ETMC results include disconnected contributions, which, although small, have a systematic effect. We observe a similar behavior as for the isovector case, namely smaller values for the electric and magnetic r.m.s radii when errors are small. LHPC results extracted using the summation method have larger errors and are thus compatible with both the muonic and electron scattering determinations of the r.m.s. radii. For the neutron radii we have only results from ETMC and LHPC. They are displayed in Fig. 32. ETMC results on the electric r.m.s. radius, which are determined at high accuracy

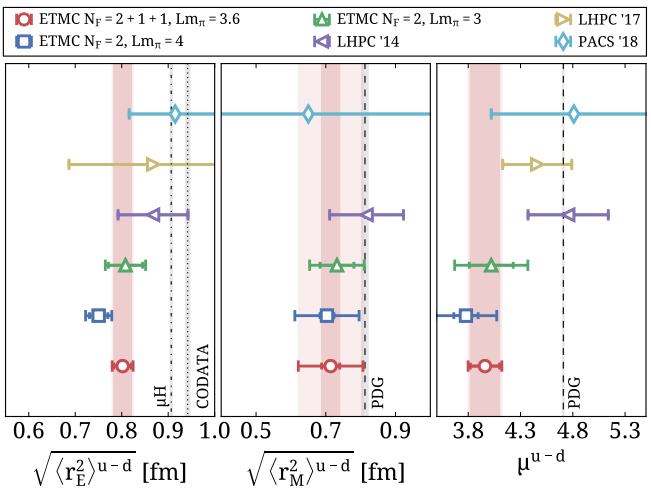

FIG. 30. Isovector $\sqrt{\langle r_E^2\rangle^{u-d}}$, $\sqrt{\langle r_M^2\rangle^{u-d}}$ and μ^{u-d} with lattice QCD results following the notation of Fig. 27. The experimental result extracted from muonic hydrogen [3] is shown by the vertical dashed-dotted line and from CODATA [65] by the dotted vertical line. The PDG value [66] is shown with the dashed vertical line. The red vertical inner band denotes the statistical error extracted using the N_f=2+1+1 twisted mass ensemble of this work and the outer lighter band is the total error adding statistical and systematic errors in quadrature.

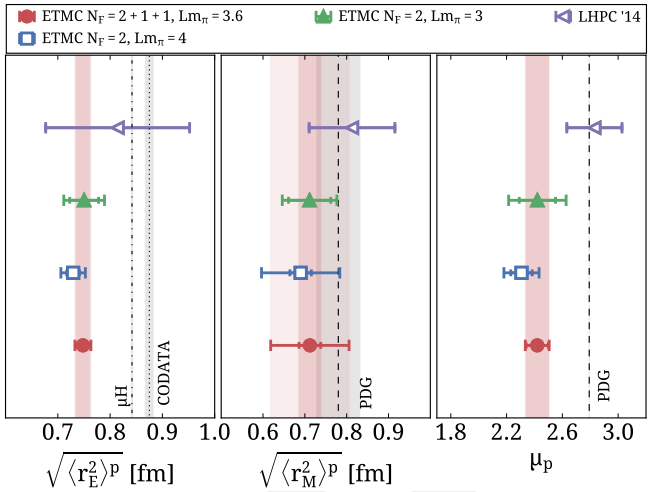

FIG. 31. Results for $\sqrt{\langle r_E^2\rangle^p}$ and $\sqrt{\langle r_M^2\rangle^p}$ using the same notation as in Fig. 30. Filled symbols denote results that include all contributions whereas open symbols are those where disconnected contributions are neglected. The rest of the notation follows that of Fig. 30.

and include all contributions, although still smaller in magnitude than the experimental values are within one standard deviation. In fact, including disconnected contributions brings better agreement in particular in the case of $\langle r_E^2\rangle^n$.

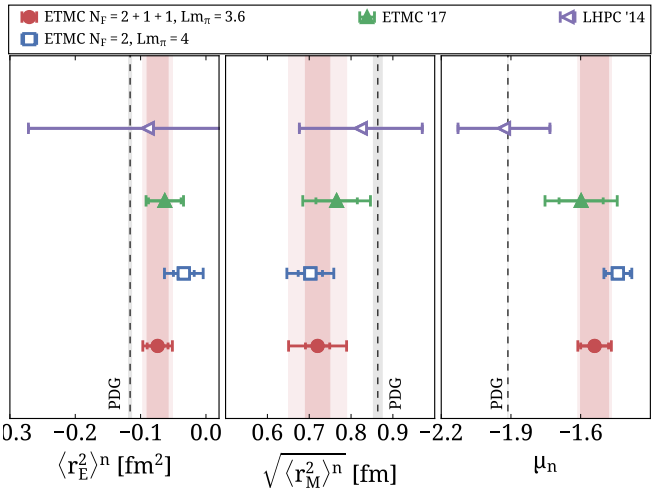

FIG. 32. Lattice QCD results for $\langle r_E^2\rangle^n$, $\sqrt{\langle r_M^2\rangle^n}$ and μ_n. The notation is as in Fig. 31.

VII. PROTON AND NEUTRON ELECTROMAGNETIC FORM FACTORS

Having compared with other groups and with N_f=2 results from ETMC, we collect here our final results on the proton and neutron form factors using the N_f=2+1+1 ensemble, which has the most accurate results at the physical point. In Fig. 33 we show our results for the proton electric and magnetic form factors compared to experimental data. As expected from the behavior observed for the isovector and isoscalar electric form factors, the proton electric form factor is consistently higher than the experimental results. The proton magnetic form factor agrees with the experiment for all Q^2 except the lowest one, which may be due to finite volume effects as discussed in Section V.

In Fig. 34 we show our results for the neutron form factors. The determination of $G_E^n(Q^2)$ directly from lattice QCD is remarkable; there is first of all good agreement with experiment but more importantly, at low Q^2, the errors from lattice QCD are smaller by up to a factor of four in some cases, allowing for a more precise description of its Q^2 dependence. The determination of $G_M^n(Q^2)$ is also very accurate yielding agreement with experiment for Q^2>0.2 GeV^2 while at small Q^2 we observe the same discrepancy as that observed for the isovector case.

Our results for the proton radii and magnetic moment, as extracted from the dipole fit, are as follows

$$\begin{aligned}\sqrt{\langle r_E^2\rangle^p} &= 0.748(13)(8)(1)\ \text{fm},\\ \mu_p &= 2.42(8)(2)(2)(^1_0),\\ \sqrt{\langle r_M^2\rangle^p} &= 0.712(26)(90)(5)(^2_0)\ \text{fm}.\end{aligned} \tag{36}$$

The corresponding quantities for the neutron using the Galster-like parameterization for the electric and the

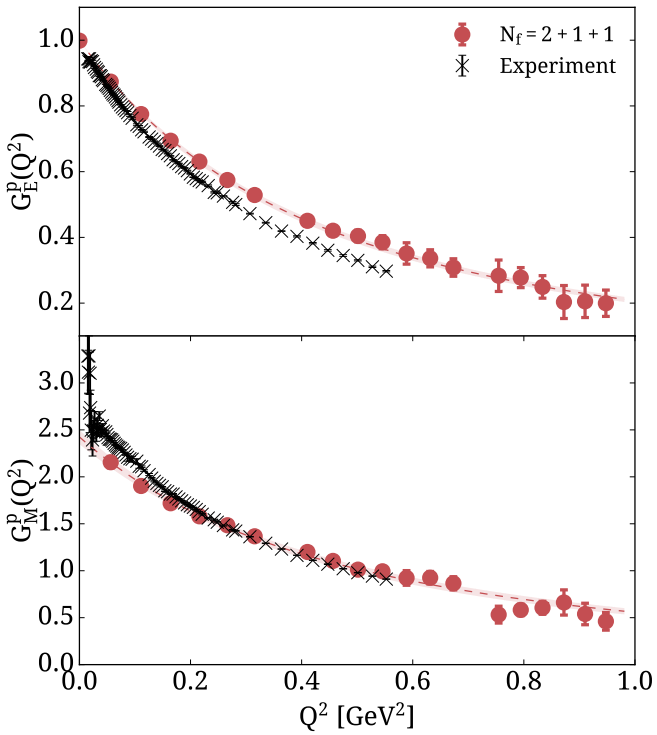

FIG. 33. Proton electric (upper panel) and magnetic (lower panel) form factors as a function of Q^2. Filled circles show the lattice QCD results of this work and black crosses are experimental results from the A1 collaboration [1]. The band is the fit to our results using Eq. (18).

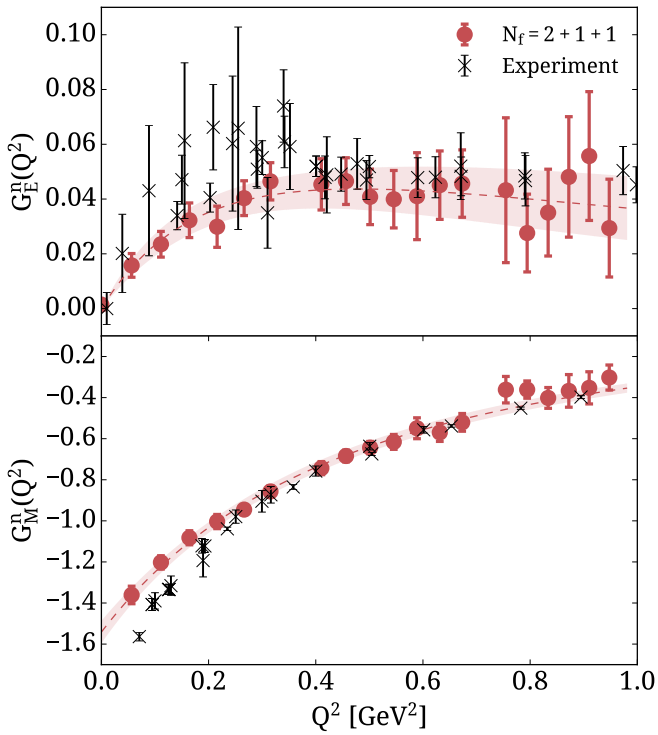

FIG. 34. Neutron electric (upper panel) and magnetic (lower panel) form factors as a function of Q^2. Filled circles show the lattice QCD results of this work and black crosses are experimental results taken from Refs. [4, 43–56] for the case of the electric form factor and from Refs. [59–64] for the case of the magnetic form factor. The fits to our results use Eq. (20) for the electric form factor and Eq. (18) for the magnetic form factors.

dipole form for the magnetic are

$$\begin{aligned} \langle r_E^2 \rangle^n &= -0.074(16)(12)(11)\ \text{fm}^2, \\ \mu_n &= -1.54(6)(1)(4), \\ \sqrt{\langle r_M^2 \rangle^n} &= 0.719(29)(60)(19)\ \text{fm}. \end{aligned} \tag{37}$$

As already explained, the first error is statistical, the second is an estimate of the systematic due to the Ansätz chosen for the fit and the third an estimate of excited state effects. We note here that disconnected contributions to $\langle r_E^2 \rangle^n$ are non-negligible. If we were to neglect them we would obtain $\langle r_E^2 \rangle^{n,conn.} = -0.064(15)$ fm^2, namely more than a 15% shift in the mean value, i.e. comparable to the other quoted systematic errors.

VIII. SUMMARY AND CONCLUSIONS

The nucleon electromagnetic Sachs form factors are computed using an N_f=2+1+1 ensemble of maximally twisted mass fermions with quark masses tuned to their physical values as well as an ensemble of N_f=2 twisted mass fermions simulated at a pion mass of 130 MeV. The novelty of this work is the computation to an unprecedented accuracy of the disconnected light quark contributions, allowing us to extract the individual proton and neutron electromagnetic form factors. This is accomplished by using state-of-the-art techniques that combine hierarchical probing and deflation of the lowest eigen-modes and a large number of randomly distributed smeared point sources in order to suppress gauge noise. In particular, we find that disconnected contributions to the neutron electric form factor are non-negligible and need to be taken into account to bring agreement with the experimental values.

Excited states are thoroughly investigated using five sink-source time separation in the range of [0.97-1.62] fm allowing the identification of the ground state to good precision and the determination of a reliable systematic error due to the excited states by comparing results from the plateau method with the two-state fit method. The summation method is used as a confirmation of the results extracted from the plateau and two-states fits.

Finite volume effects are investigated by comparing two N_f=2 twisted mass ensembles with pion mass of 130 MeV with the same lattice spacing but $Lm_\pi \simeq 3$ and $Lm_\pi \simeq 4$. We observe consistent results between these two volumes, but we cannot exclude finite volume effects that may affect the magnetic form factor for small Q^2 values. Further studies are required to take the infinite volume limit and make definite conclusions on the small Q^2 behavior of the magnetic form factor. Comparing

results calculated using N_f=2 and N_f=2+1+1 twisted mass ensembles we observed no quenching effects. Our values for the electric and magnetic r.m.s. radii as well as the magnetic moments for the isovector, isoscalar, proton and neutron are collected in Table V. The results

TABLE V. Our results for the electromagnetic radii and the magnetic moment using the N_f=2+1+1 ensemble for the isovector combination ($p-n$), isoscalar ($p+n$), the proton and neutron. The first error is statistical, the second is a systematic due to the fit Ansätz, and the third a systematic due to excited states, derived as explained in the text.

	$\sqrt{\langle r_E^2\rangle}$ [fm]	$\sqrt{\langle r_M^2\rangle}$ [fm]	μ
$p-n$	0.802(19)(12)(1)	0.714(26)(88)(16)	3.96(14)(3)(7)
$p+n$	0.697(9)(10)(0)	0.695(37)(108)(3)	0.88(4)(4)(2)
p	0.748(13)(8)(1)	0.712(26)(90)(5)	2.42(8)(2)(2)
n	$\langle r_E^2\rangle$ [fm^2] -0.074(16)(12)(11)	0.720(29)(60)(19)	-1.54(6)(1)(4)

are extracted using the dipole ansätz or the Galster-like parameterization and a systematic error on the parameterization used is extracted by comparing with the model independent z-expansion. Our result for the proton electric r.m.s radius is underestimated due to the slower decay of $G_E^p(Q^2)$ and further studies are required in order for lattice QCD results to reach an accuracy that can distinguish between the experimental results for the proton charge radius.

ACKNOWLEDGMENTS

We would like to thank all members of ETMC for a very constructive and enjoyable collaboration. M.C. acknowledges financial support by the U.S. National Science Foundation under Grant No. PHY-1714407. This project has received funding from the Horizon 2020 research and innovation program of the European Commission under the Marie Skłodowska-Curie grant agreement No 642069. S.B. is supported by this program. The authors gratefully acknowledge the Gauss Centre for Supercomputing e.V. (www.gauss-centre.eu) for funding the project pr74yo by providing computing time on the GCS Supercomputer SuperMUC at Leibniz Supercomputing Centre (www.lrz.de). Results were obtained using Piz Daint at Centro Svizzero di Calcolo Scientifico (CSCS), via the project with id s702. We thank the staff of CSCS for access to the computational resources and for their constant support. This work also used computational resources from Extreme Science and Engineering Discovery Environment (XSEDE), which is supported by National Science Foundation grant number TG-PHY170022. This work used computational resources from the John von Neumann-Institute for Computing on the Jureca system at the research center in Jülich, under the project with id ECY00.

[1] J. C. Bernauer et al. Electric and magnetic form factors of the proton. *Phys. Rev.*, C90(1):015206, 2014. doi: 10.1103/PhysRevC.90.015206.

[2] V. Punjabi, C. F. Perdrisat, M. K. Jones, E. J. Brash, and C. E. Carlson. The Structure of the Nucleon: Elastic Electromagnetic Form Factors. *Eur. Phys. J.*, A51:79, 2015. doi:10.1140/epja/i2015-15079-x.

[3] Randolf Pohl et al. The size of the proton. *Nature*, 466: 213–216, 2010. doi:10.1038/nature09250.

[4] J. Golak, G. Ziemer, H. Kamada, H. Witala, and Walter Gloeckle. Extraction of electromagnetic neutron formfactors through inclusive and exclusive polarized electron scattering on polarized He-3 target. *Phys. Rev.*, C63: 034006, 2001. doi:10.1103/PhysRevC.63.034006.

[5] Constantia Alexandrou et al. Simulating twisted mass fermions at physical light, strange and charm quark masses. 2018.

[6] C. Alexandrou, M. Constantinou, K. Hadjiyiannakou, K. Jansen, C. Kallidonis, G. Koutsou, and A. Vaquero Avilés-Casco. Strange nucleon electromagnetic form factors from lattice QCD. *Phys. Rev.*, D97(9):094504, 2018. doi:10.1103/PhysRevD.97.094504.

[7] Constantia Alexandrou, Martha Constantinou, Kyriakos Hadjiyiannakou, Karl Jansen, Christos Kallidonis, Giannis Koutsou, and Alejandro Vaquero Aviles-Casco. Nucleon electromagnetic form factors using lattice simulations at the physical point. *Phys. Rev.*, D96(3):034503, 2017. doi:10.1103/PhysRevD.96.034503.

[8] S. Galster, H. Klein, J. Moritz, K. H. Schmidt, D. Wegener, and J. Bleckwenn. Elastic electron-deuteron scattering and the electric neutron form factor at four-momentum transfers 5fm$^{-2} < q^2 <$ 14fm^{-2}. *Nucl. Phys.*, B32:221–237, 1971. doi:10.1016/0550-3213(71)90068-X.

[9] Richard J. Hill and Gil Paz. Model independent extraction of the proton charge radius from electron scattering. *Phys. Rev.*, D82:113005, 2010. doi: 10.1103/PhysRevD.82.113005.

[10] Andreas Stathopoulos, Jesse Laeuchli, and Kostas Orginos. Hierarchical probing for estimating the trace of the matrix inverse on toroidal lattices. 2013.

[11] Arjun Singh Gambhir, Andreas Stathopoulos, and Kostas Orginos. Deflation as a Method of Variance Reduction for Estimating the Trace of a Matrix Inverse. *SIAM J. Sci. Comput.*, 39:A532–A558, 2017. doi: 10.1137/16M1066361.

[12] S. Capitani, M. Della Morte, D. Djukanovic, G. von Hippel, J. Hua, B. Jager, B. Knippschild, H. B. Meyer, T. D. Rae, and H. Wittig. Nucleon electromagnetic form factors in two-flavor QCD. *Phys. Rev.*, D92(5):054511, 2015. doi:10.1103/PhysRevD.92.054511.

[13] J. R. Green, J. W. Negele, A. V. Pochinsky, S. N. Syritsyn, M. Engelhardt, and S. Krieg. Nucleon electromagnetic form factors from lattice QCD using a nearly physical pion mass. *Phys. Rev.*, D90:074507, 2014. doi:

10.1103/PhysRevD.90.074507.

[14] Nesreen Hasan, Jeremy Green, Stefan Meinel, Michael Engelhardt, Stefan Krieg, John Negele, Andrew Pochinsky, and Sergey Syritsyn. Computing the nucleon charge and axial radii directly at $Q^2 = 0$ in lattice QCD. *Phys. Rev.*, D97(3):034504, 2018. doi: 10.1103/PhysRevD.97.034504.

[15] Ken-Ichi Ishikawa, Yoshinobu Kuramashi, Shoichi Sasaki, Natsuki Tsukamoto, Akira Ukawa, and Takeshi Yamazaki. Nucleon form factors on a large volume lattice near the physical point in 2+1 flavor QCD. *Phys. Rev.*, D98(7):074510, 2018. doi:10.1103/PhysRevD.98.074510.

[16] S. Gusken. A Study of smearing techniques for hadron correlation functions. *Nucl. Phys. Proc. Suppl.*, 17:361–364, 1990. doi:10.1016/0920-5632(90)90273-W.

[17] C. Alexandrou, S. Gusken, F. Jegerlehner, K. Schilling, and R. Sommer. The Static approximation of heavy - light quark systems: A Systematic lattice study. *Nucl. Phys.*, B414:815–855, 1994. doi:10.1016/0550-3213(94)90262-3.

[18] M. Albanese et al. Glueball Masses and String Tension in Lattice QCD. *Phys. Lett.*, B192:163–169, 1987. doi: 10.1016/0370-2693(87)91160-9.

[19] C. Alexandrou, M. Constantinou, S. Dinter, V. Drach, K. Jansen, C. Kallidonis, and G. Koutsou. Nucleon form factors and moments of generalized parton distributions using $N_f = 2 + 1 + 1$ twisted mass fermions. *Phys. Rev.*, D88(1):014509, 2013. doi:10.1103/PhysRevD.88.014509.

[20] C. Alexandrou, M. Brinet, J. Carbonell, M. Constantinou, P. A. Harraud, P. Guichon, K. Jansen, T. Korzec, and M. Papinutto. Nucleon electromagnetic form factors in twisted mass lattice QCD. *Phys. Rev.*, D83:094502, 2011. doi:10.1103/PhysRevD.83.094502.

[21] C. Alexandrou, G. Koutsou, John W. Negele, and A. Tsapalis. The Nucleon electromagnetic form factors from Lattice QCD. *Phys. Rev.*, D74:034508, 2006. doi: 10.1103/PhysRevD.74.034508.

[22] Simone Bacchio, Constantia Alexandrou, and Jacob Finkerath. Multigrid accelerated simulations for Twisted Mass fermions. *EPJ Web Conf.*, 175:02002, 2018. doi: 10.1051/epjconf/201817502002.

[23] Simone Bacchio, Costantia Alexandrou, Jacob Finkenrath, Andreas Frommer, Karsten Kahl, and Matthias Rottmann. DDalphaAMG for Twisted Mass Fermions. *PoS*, LATTICE2016:259, 2016.

[24] Constantia Alexandrou, Simone Bacchio, Jacob Finkenrath, Andreas Frommer, Karsten Kahl, and Matthias Rottmann. Adaptive Aggregation-based Domain Decomposition Multigrid for Twisted Mass Fermions. *Phys. Rev.*, D94(11):114509, 2016. doi: 10.1103/PhysRevD.94.114509.

[25] Walter Wilcox. Noise methods for flavor singlet quantities. In *Numerical challenges in lattice quantum chromodynamics. Proceedings, Joint Interdisciplinary Workshop, Wuppertal, Germany, August 22-24, 1999*, pages 127–141, 1999.

[26] Jeremy Green, Stefan Meinel, Michael Engelhardt, Stefan Krieg, Jesse Laeuchli, John Negele, Kostas Orginos, Andrew Pochinsky, and Sergey Syritsyn. High-precision calculation of the strange nucleon electromagnetic form factors. *Phys. Rev.*, D92(3):031501, 2015. doi: 10.1103/PhysRevD.92.031501.

[27] Jeremy Green, Nesreen Hasan, Stefan Meinel, Michael Engelhardt, Stefan Krieg, Jesse Laeuchli, John Negele, Kostas Orginos, Andrew Pochinsky, and Sergey Syritsyn. Up, down, and strange nucleon axial form factors from lattice QCD. *Phys. Rev.*, D95(11):114502, 2017. doi: 10.1103/PhysRevD.95.114502.

[28] C. McNeile and Christopher Michael. Decay width of light quark hybrid meson from the lattice. *Phys. Rev.*, D73:074506, 2006. doi:10.1103/PhysRevD.73.074506.

[29] C. Alexandrou, M. Constantinou, V. Drach, K. Hadjiyiannakou, K. Jansen, G. Koutsou, A. Strelchenko, and A. Vaquero. Evaluation of disconnected quark loops for hadron structure using GPUs. *Comput. Phys. Commun.*, 185:1370–1382, 2014. doi:10.1016/j.cpc.2014.01.009.

[30] Constantia Alexandrou, Martha Constantinou, Kyriakos Hadjiyiannakou, Karl Jansen, Christos Kallidonis, Giannis Koutsou, and Alejandro Vaquero Aviles-Casco. Nucleon axial form factors using $N_f = 2$ twisted mass fermions with a physical value of the pion mass. *Phys. Rev.*, D96(5):054507, 2017. doi: 10.1103/PhysRevD.96.054507.

[31] C. Alexandrou et al. Nucleon scalar and tensor charges using lattice QCD simulations at the physical value of the pion mass. *Phys. Rev.*, D95(11): 114514, 2017. doi:10.1103/PhysRevD.96.099906, 10.1103/PhysRevD.95.114514. [Erratum: Phys. Rev.D96,no.9,099906(2017)].

[32] C. Alexandrou, M. Constantinou, K. Hadjiyiannakou, K. Jansen, C. Kallidonis, G. Koutsou, A. Vaquero Avilés-Casco, and C. Wiese. Nucleon Spin and Momentum Decomposition Using Lattice QCD Simulations. *Phys. Rev. Lett.*, 119(14):142002, 2017. doi: 10.1103/PhysRevLett.119.142002.

[33] R. Frezzotti and G. C. Rossi. Chirally improving Wilson fermions. 1. O(a) improvement. *JHEP*, 08:007, 2004. doi: 10.1088/1126-6708/2004/08/007.

[34] R. Frezzotti and G. C. Rossi. Twisted mass lattice QCD with mass nondegenerate quarks. *Nucl. Phys. Proc. Suppl.*, 128:193–202, 2004. doi:10.1016/S0920-5632(03)02477-0. [,193(2003)].

[35] A. Abdel-Rehim et al. First physics results at the physical pion mass from $N_f = 2$ Wilson twisted mass fermions at maximal twist. *Phys. Rev.*, D95(9):094515, 2017. doi: 10.1103/PhysRevD.95.094515.

[36] L. Maiani, G. Martinelli, M. L. Paciello, and B. Taglienti. Scalar Densities and Baryon Mass Differences in Lattice QCD With Wilson Fermions. *Nucl. Phys.*, B293: 420, 1987. doi:10.1016/0550-3213(87)90078-2.

[37] S. Capitani, M. Della Morte, G. von Hippel, B. Jager, A. Juttner, B. Knippschild, H. B. Meyer, and H. Wittig. The nucleon axial charge from lattice QCD with controlled errors. *Phys. Rev.*, D86:074502, 2012. doi: 10.1103/PhysRevD.86.074502.

[38] Martin J. Savage, Phiala E. Shanahan, Brian C. Tiburzi, Michael L. Wagman, Frank Winter, Silas R. Beane, Emmanuel Chang, Zohreh Davoudi, William Detmold, and Kostas Orginos. Proton-Proton Fusion and Tritium β Decay from Lattice Quantum Chromodynamics. *Phys. Rev. Lett.*, 119(6):062002, 2017. doi: 10.1103/PhysRevLett.119.062002.

[39] C. F. Perdrisat, V. Punjabi, and M. Vanderhaeghen. Nucleon Electromagnetic Form Factors. *Prog. Part. Nucl. Phys.*, 59:694–764, 2007. doi:10.1016/j.ppnp.2007.05.001.

[40] W. M. Alberico, S. M. Bilenky, C. Giunti, and K. M. Graczyk. Electromagnetic form factors of the nucleon: New Fit and analysis of uncertainties. *Phys. Rev.*, C79:

065204, 2009. doi:10.1103/PhysRevC.79.065204.
[41] Constantia Alexandrou, Martha Constantinou, and Haralambos Panagopoulos. Renormalization functions for Nf=2 and Nf=4 twisted mass fermions. *Phys. Rev.*, D95 (3):034505, 2017. doi:10.1103/PhysRevD.95.034505.
[42] C. Alexandrou, M. Constantinou, T. Korzec, H. Panagopoulos, and F. Stylianou. Renormalization constants for 2-twist operators in twisted mass QCD. *Phys. Rev.*, D83:014503, 2011. doi: 10.1103/PhysRevD.83.014503.
[43] J. Becker et al. Determination of the neutron electric form-factor from the reaction He-3(e,e' n) at medium momentum transfer. *Eur. Phys. J.*, A6:329–344, 1999. doi:10.1007/s100500050351.
[44] T. Eden et al. Electric form factor of the neutron from the ${}^2H(\overrightarrow{e}, e?\overrightarrow{n})^1H$ reaction at $Q^2 = 0.255$ $(\mathrm{GeV/c})^2$. *Phys. Rev.*, C50(4):R1749–R1753, 1994. doi: 10.1103/PhysRevC.50.R1749.
[45] M. Meyerhoff et al. First measurement of the electric form-factor of the neutron in the exclusive quasielastic scattering of polarized electrons from polarized He-3. *Phys. Lett.*, B327:201–207, 1994. doi:10.1016/0370-2693(94)90718-8.
[46] I. Passchier et al. The Charge form-factor of the neutron from the reaction polarized H-2(polarized e, e-prime n) p. *Phys. Rev. Lett.*, 82:4988–4991, 1999. doi: 10.1103/PhysRevLett.82.4988.
[47] G. Warren et al. Measurement of the electric form-factor of the neutron at $Q^2 = 0.5$ and 1.0 GeV^2/c^2. *Phys. Rev. Lett.*, 92:042301, 2004. doi: 10.1103/PhysRevLett.92.042301.
[48] H. Zhu et al. A Measurement of the electric form-factor of the neutron through polarized-d (polarized-e, e-prime n)p at Q**2 = 0.5-(GeV/c)**2. *Phys. Rev. Lett.*, 87: 081801, 2001. doi:10.1103/PhysRevLett.87.081801.
[49] B. Plaster et al. Measurements of the neutron electric to magnetic form-factor ratio G(En) / G(Mn) via the H-2(polarized-e, e-prime,polarized-n)H-1 reaction to Q**2 = 1.45-(GeV/c)**2. *Phys. Rev.*, C73:025205, 2006. doi: 10.1103/PhysRevC.73.025205.
[50] R. Madey et al. Measurements of G(E)n / G(M)n from the H-2(polarized-e,e-prime polarized-n) reaction to Q**2 = 1.45 (GeV/c)**2. *Phys. Rev. Lett.*, 91:122002, 2003. doi:10.1103/PhysRevLett.91.122002.
[51] D. Rohe et al. Measurement of the neutron electric form-factor G(en) at 0.67-(GeV/c)**2 via He-3(pol.)(e(pol.),e' n). *Phys. Rev. Lett.*, 83:4257–4260, 1999. doi: 10.1103/PhysRevLett.83.4257.
[52] J. Bermuth et al. The Neutron charge form-factor and target analyzing powers from polarized-He-3 (polarized-e,e-prime n) scattering. *Phys. Lett.*, B564:199–204, 2003. doi:10.1016/S0370-2693(03)00725-1.
[53] D. I. Glazier et al. Measurement of the electric form-factor of the neutron at Q**2 = 0.3-(GeV/c)**2 to 0.8-(GeV/c)**2. *Eur. Phys. J.*, A24:101–109, 2005. doi: 10.1140/epja/i2004-10115-8.
[54] C. Herberg et al. Determination of the neutron electric form-factor in the D(e,e' n)p reaction and the influence of nuclear binding. *Eur. Phys. J.*, A5:131–135, 1999. doi: 10.1007/s100500050268.
[55] R. Schiavilla and I. Sick. Neutron charge form-factor at large q**2. *Phys. Rev.*, C64:041002, 2001. doi: 10.1103/PhysRevC.64.041002.
[56] M. Ostrick et al. Measurement of the neutron electric form-factor G(E,n) in the quasifree H-2(e(pol.),e' n(pol.))p reaction. *Phys. Rev. Lett.*, 83:276–279, 1999. doi:10.1103/PhysRevLett.83.276.
[57] Toru Sato, D. Uno, and T. S. H. Lee. Dynamical model of weak pion production reactions. *Phys. Rev.*, C67:065201, 2003. doi:10.1103/PhysRevC.67.065201.
[58] Eigo Shintani, Ken-Ichi Ishikawa, Yoshinobu Kuramashi, Shoichi Sasaki, and Takeshi Yamazaki. Nucleon form factors and root-mean-square radii on a $(10.8\ \mathrm{fm})^4$ lattice at the physical point. 2018.
[59] B. Anderson et al. Extraction of the neutron magnetic form-factor from quasi-elastic polarized-He-3(polarized-e, e-prime) at Q**2=0.1 - 0.6 (GeV/c)**2. *Phys. Rev.*, C75:034003, 2007. doi:10.1103/PhysRevC.75.034003.
[60] H. Gao et al. Measurement of the neutron magnetic form-factor from inclusive quasielastic scattering of polarized electrons from polarized He-3. *Phys. Rev.*, C50:R546–R549, 1994. doi:10.1103/PhysRevC.50.R546.
[61] H. Anklin et al. Precision measurement of the neutron magnetic form-factor. *Phys. Lett.*, B336:313–318, 1994. doi:10.1016/0370-2693(94)90538-X.
[62] H. Anklin et al. Precise measurements of the neutron magnetic form-factor. *Phys. Lett.*, B428:248–253, 1998. doi:10.1016/S0370-2693(98)00442-0.
[63] G. Kubon et al. Precise neutron magnetic form-factors. *Phys. Lett.*, B524:26–32, 2002. doi:10.1016/S0370-2693(01)01386-7.
[64] R. Alarcon. Nucleon form factors and the BLAST experiment. *Eur. Phys. J.*, A32(4):477–481, 2007. doi: 10.1140/epja/i2006-10395-x, 10.1140/epja/i2006-10268-4. [Eur. Phys. J.A32,477(2007)].
[65] Peter J. Mohr, David B. Newell, and Barry N. Taylor. CODATA Recommended Values of the Fundamental Physical Constants: 2014. *Rev. Mod. Phys.*, 88(3): 035009, 2016. doi:10.1103/RevModPhys.88.035009.
[66] C. Patrignani et al. Review of Particle Physics. *Chin. Phys.*, C40(10):100001, 2016. doi:10.1088/1674-1137/40/10/100001.

Appendix A: Expressions relating nucleon vector matrix elements to electromagnetic form factors

In this Appendix we give a summary of the expressions relating the Sachs form factors $G_E{\equiv}G_E(Q^2)$ and $G_M{\equiv}G_M(Q^2)$ to the ratio of three-point and two-point functions. The expressions are given for a general frame with initial (final) momentum $\vec{p}$ ($\vec{p}'$) and initial (final) energy E (E'). All expressions are given in Euclidean space.

$$\Pi_\mu(\Gamma_0,\vec{p}\,',\vec{p}) = \frac{-iC\,G_E}{2m(4m^2+Q^2)}\left((p'_\mu+p_\mu)\left[m\,(E'+E+m)-p'_\rho p_\rho\right]\right)$$
$$+\frac{C\,G_M}{4m^2(4m^2+Q^2)}\Big(\delta_{\mu 0}\big(4m^4+m^2Q^2+4m^2p'_\rho p_\rho+Q^2p'_\rho p_\rho\big)$$
$$+2im^2p'_\mu\big(E'-E\big)-2im^3(p'_\mu+p_\mu)-iEQ^2p'_\mu-iE'Q^2p_\mu$$
$$-imQ^2(p'_\mu+p_\mu)-2im^2p_\mu\big(E'-E\big)-2imp'_\rho p_\rho(p'_\mu+p_\mu)\Big)\,, \tag{A1}$$

$$\Pi_\mu(\Gamma_k,\vec{p}\,',\vec{p}) = \frac{-C\,G_E}{2m(4m^2+Q^2)}\Big(m^2\,\varepsilon_{\mu k0\rho}(p'_\rho-p_\rho)-i\,\varepsilon_{\mu k\rho\sigma}p'_\rho p_\sigma\big(E'+E\big)$$
$$+\varepsilon_{\mu 0\rho\sigma}p'_\rho p_\sigma(p'_k+p_k)-\varepsilon_{\mu k0\rho}p'_\sigma p_\sigma(p'_\rho-p_\rho)\Big)$$
$$-\frac{C\,G_M}{4m^2(4m^2+Q^2)}\Big(m\,\varepsilon_{\mu k0\rho}(p'_\rho-p_\rho)(2m^2+Q^2)$$
$$+2im\,\varepsilon_{\mu k\rho\sigma}p'_\rho p_\sigma\big(2m+E'+E+\frac{Q^2}{2m}\big)$$
$$-2m\,\varepsilon_{\mu 0\rho\sigma}p'_\rho p_\sigma(p'_k+p_k)+2m\,\varepsilon_{\mu k0\rho}p'_\sigma p_\sigma(p'_\rho-p_\rho)\Big), \tag{A2}$$

where C is a kinematic factor given by

$$C=\frac{2m}{E(E(\vec{p}\,')+m)}\sqrt{\frac{E(E(\vec{p}\,')+m)}{E(\vec{p}\,')(E+m)}}\,. \tag{A3}$$

In the case where $\vec{p}\,'=\vec{0}$ the expressions simplify as follows

$$\Pi_0(\Gamma_0,\vec{p})=C\frac{E+m}{2m}G_E(Q^2), \tag{A4}$$

$$\Pi_i(\Gamma_0,\vec{p})=C\frac{p_i}{2m}G_E(Q^2), \tag{A5}$$

$$\Pi_i(\Gamma_k,\vec{p})=C\frac{\epsilon_{ijk}p_j}{2m}G_M(Q^2) \tag{A6}$$

and

$$C=\sqrt{\frac{2m^2}{E(E+m)}}\,. \tag{A7}$$

Appendix B: Numerical results for the electromagnetic form factors

TABLE VI. Results for the electromagnetic form factors for the isovector combination $G^p_{E,M} - G^n_{E,M}$, for the proton $G^p_{E,M}$ and neutron $G^n_{E,M}$, including the disconnected contributions for the latter two form factors.

$Q^2[GeV^2]$	$G_E^{p-n}(Q^2)$	$G^p_E(Q^2)$	$G^n_E(Q^2)$	$G_M^{u-d}(Q^2)$	$G^p_M(Q^2)$	$G^n_M(Q^2)$
0.000	0.997(3)	0.998(2)	0.001(1)	NA	NA	NA
0.056	0.858(10)	0.874(6)	0.016(5)	3.516(101)	2.156(62)	-1.361(43)
0.111	0.752(11)	0.775(8)	0.023(5)	3.105(78)	1.903(48)	-1.202(33)
0.164	0.662(14)	0.694(9)	0.032(7)	2.801(80)	1.719(47)	-1.082(35)
0.216	0.601(17)	0.631(10)	0.030(8)	2.583(82)	1.580(50)	-1.003(35)
0.266	0.534(14)	0.575(9)	0.040(7)	2.430(62)	1.485(38)	-0.945(26)
0.315	0.482(16)	0.529(11)	0.046(7)	2.224(70)	1.367(43)	-0.857(29)
0.410	0.405(23)	0.450(16)	0.045(10)	1.943(78)	1.200(48)	-0.743(32)
0.456	0.374(21)	0.420(15)	0.047(9)	1.789(71)	1.104(44)	-0.684(29)
0.501	0.363(25)	0.404(18)	0.041(11)	1.655(69)	1.012(42)	-0.644(31)
0.546	0.345(27)	0.385(21)	0.040(11)	1.610(84)	0.994(50)	-0.616(37)
0.589	0.310(43)	0.351(33)	0.041(16)	1.472(127)	0.923(79)	-0.549(51)
0.631	0.291(33)	0.336(27)	0.045(13)	1.495(109)	0.926(67)	-0.570(44)
0.673	0.263(34)	0.308(27)	0.046(13)	1.386(112)	0.866(71)	-0.521(44)
0.755	0.239(60)	0.283(48)	0.043(27)	0.893(149)	0.532(90)	-0.361(65)
0.794	0.250(39)	0.278(31)	0.028(15)	0.942(101)	0.583(62)	-0.361(43)
0.834	0.213(43)	0.249(35)	0.035(16)	1.006(117)	0.605(70)	-0.402(51)
0.872	0.158(61)	0.203(51)	0.048(22)	1.028(211)	0.662(135)	-0.367(80)
0.910	0.150(58)	0.205(50)	0.056(24)	0.891(190)	0.539(115)	-0.353(79)
0.948	0.172(48)	0.200(41)	0.029(18)	0.765(153)	0.461(94)	-0.302(61)